**Table 1** Effects of G-CSF on the incidence of VF during reperfusion periods

| Group | Incidence of VF (%) | |
|---|---|---|
| Control | 50.0 | (4/8) |
| G-CSF | 0* | (0/6) |
| G-CSF + WTMN | 42.9 | (3/7) |
| WTMN | 50.0 | (3/6) |

*$p < 0.05$ vs. control group

### Effect of G-CSF on Akt phosphorylation in ischemic myocardium

G-CSF augmented Akt phosphrylation in the LAD-perfused myocardium. The increase in Akt phosphorylation was attenuated by wortmannin (Fig. 5).

## Discussion

The present study demonstrated that administration of G-CSF following the onset of reperfusion limited infarct size in acute phase and reduced the incidence of lethal arrhythmia. The intracoronary administration of wortmannin abrogated these cardioprotective effects of G-CSF, suggesting that G-CSF mediated cardioprotection via the PI3K/Akt pathway. To our knowledge, this is the first study to reveal the acute effect of G-CSF against ischemia/reperfusion injury via the PI3K/Akt pathway in in vivo canine hearts.

Previous studies have reported that G-CSF improves cardiac remodeling after MI in the chronic ligation model of coronary artery [4, 5, 16]. It has been believed that G-CSF exerts cardioprotective effects through regeneration of myocardium and angiogenesis. Recently, Komuro and colleagues clearly demonstrated that the high dose of G-CSF limits infarct size in the acute phase in the isolated hearts [6]. To translate their remarkable findings into the clinical setting, we need to consider the dose of G-CSF and experimental models in their study. They used a perfusate containing 300 ng/ml G-CSF in the isolated heart model. This dose is relatively high compared with the dose used in clinical settings [17, 18]. In addition, effects of G-CSF on neutrophil function cannot be tested in the isolated heart model. In the present study, we demonstrated that a clinical relevant dose of G-CSF acutely limits infarct size in the in vivo model. In contrast with previous studies [4, 5, 16], we examined the effects of G-CSF in the ischemia/reperfusion model, because coronary revascularization is principally applied for patients with acute MI to attenuate ischemia/reperfusion injury. We found that G-CSF following the onset of reperfusion effectively limited infarct size. Our findings strongly support that G-CSF would be a promising candidate as an adjunctive therapy for patients with acute MI. Indeed, two recent publications by the FIRSTLINE-AMI trial clearly demonstrated that subcutaneous administration of G-CSF after percutaneous coronary intervention improved cardiac function and prevented cardiac remodeling [19, 20]. Considering our present data, the improvement of cardiac function by G-CSF in clinical studies will be due to limiting infarct size in the acute phase as well as preventing cardiac remodeling.

G-CSF can provoke multiple intracellular signal transductions including Jak/Stat, ERK and PI3K/Akt [16, 21]. Recently, we and others demonstrated that post-interventions which activate PI3K/Akt during the reperfusion protect against ischemia/reprfusion injury [10, 22]. Thus, we investigated a role of PI3K/Akt in G-CSF-mediated cardioprotection. WTMN significantly blunted the infarct size-limiting effects of G-CSF, and G-CSF enhanced Akt phosphorylation in the ischemic myocardium, indicating that G-CSF reduces infarct size via PI3K/Akt-dependent pathway. Further investigations will be needed to clarify the molecular target of PI3K/Akt and the role of other signals activated by G-CSF in this condition.

Although we demonstrated that G-CSF mediated cardioprotection, one small clinical study showed that G-CSF may induce coronary re-stenosis [23]. In contrast, other large-scale studies did not show that G-CSF induced coronary restenosis [19, 20]. Since there is still controversy about the restenosis effects of G-

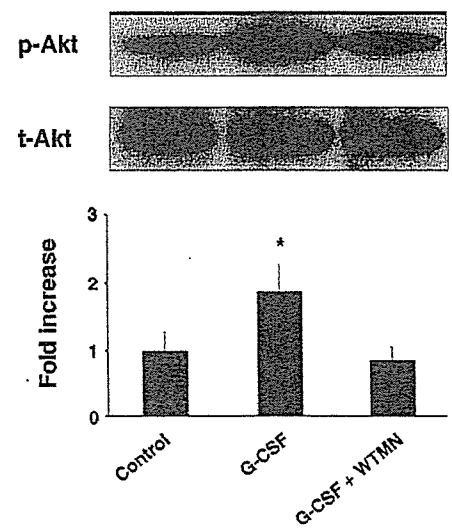


**Fig. 5** Akt phosphorylation in LAD-perfused areas. G-CSF phosphorylated Akt in LAD-perfused myocardium. Akt phosphorylation by G-CSF was prevented by co-treatment with WTMN. Akt phosphorylation was normalized by total Akt. *$p < 0.05$ vs. control group.

CSF, this issue will be minimized by the concomitant use of a drug-eluting stent and G-CSF. Another possible adverse effect of G-CSF will be enhancement of neutrophil function. G-CSF appears not only to stimulate the formation of granulocyte colonies from bone marrow-derived precursors, but also to enhance the function of mature neutrophils [24] and elevates the number of white blood cells, which may predict adverse prognosis in the patients of acute MI [25]. Consistent with previous studies [26, 27], we also showed that G-CSF did not change MPO activity, a marker of neutrophil accumulation, in the infarcted myocardium. These findings suggest that G-CSF exerted cardioprotective effects independent of white blood cells. Although our findings suggest that the overall effect of G-CSF may be beneficial for ischemia/reperfused myocardium, we need to be cautious about these potential adverse effects of G-CSF.

Importantly, we clearly demonstrated that G-CSF reduced the incidence of VF during reperfusion via the PI3/Akt-dependent pathway. Since lethal arrhythmias are one of the major causes of death in patients with acute MI [8], the anti-arrhythmic effects of G-CSF have great clinical impact. We have previously demonstrated that another cytokine, erythropoietin, also reduced the incidence of lethal arrhythmia via the PI3/Akt pathway [10]. Although our findings suggest that the PI3K/Akt-dependent pathway will play an important role in the generation of lethal arrhythmias, further investigation will be needed to clarify the potential mechanism by which G-CSF exerts anti-arrhythmic effects. We need to consider whether G-CSF exerts anti-arrhythmic effects by the reduction of myocardial infarct size or by some other actions of G-CSF.

In conclusion, the intravenous administration of a clinically relevant dose of G-CSF will be a promising strategy to treat patients with acute MI. Further controlled studies will be warranted to check the safety and efficacy of G-CSF treatment in the acute phase after MI.

**Acknowledgments** We thank Yuko Okuda, and Yoko Nagamachi for their technical assistance.

## References

1. Clark SC, Kamen R. The human hematopoietic colony-stimulating factors. Science 1987;236:1229–37.
2. To LB, Haylock DN, Simmons PJ, Juttner CA. The biology and clinical uses of blood stem cells. Blood 1997;89:2233–58.
3. Kronenwett R, Martin S, Haas R. The role of cytokines and adhesion molecules for mobilization of peripheral blood stem cells. Stem Cells 2000;18:320–30.
4. Orlic D, Kajstura J, Chimenti S, et al. Mobilized bone marrow cells repair the infarcted heart, improving function and survival. Proc Natl Acad Sci USA 2001;98:10344–9.
5. Ohtsuka M, Takano H, Zou Y, et al. Cytokine therapy prevents left ventricular remodeling and dysfunction after myocardial infarction through neovascularization. Faseb J 2004;18:851–3.
6. Harada M, Qin Y, Takano H, et al. G-CSF prevents cardiac remodeling after myocardial infarction by activating the Jak-Stat pathway in cardiomyocytes. Nat Med 2005;11:305–11.
7. Nicod P, Gilpin E, Dittrich H, et al. Late clinical outcome in patients with early ventricular fibrillation after myocardial infarction. J Am Coll Cardiol 1988;11:464–70.
8. Rouleau JL, Talajic M, Sussex B, et al. Myocardial infarction patients in the 1990s—their risk factors, stratification and survival in Canada: the Canadian Assessment of Myocardial Infarction (CAMI) Study. J Am Coll Cardiol 1996;27:1119–27.
9. Lothrop CD Jr, Warren DJ, Souza LM, Jones JB, Moore MA. Correction of canine cyclic hematopoiesis with recombinant human granulocyte colony-stimulating factor. Blood 1988;72:1324–8.
10. Hirata A, Minamino T, Asanuma H, et al. Erythropoietin just before reperfusion reduces both lethal arrhythmias and infarct size via the phosphatidylinositol-3 kinase-dependent pathway in canine hearts. Cardiovasc Drugs Ther 2005;19:33–40.
11. Maruyama R, Takemura G, Aoyama T, et al. Dynamic process of apoptosis in adult rat cardiomyocytes analyzed using 48-hour videomicroscopy and electron microscopy: beating and rate are associated with the apoptotic process. Am J Pathol 2001;159:683–91.
12. Asanuma H, Kitakaze M, Funaya H, et al. Nifedipine limits infarct size via NO-dependent mechanisms in dogs. Basic Res Cardiol 2001;96:497–505.
13. Holm S. A simple sequentially rejective multiple test procedure. Scand J Statist 1979;6:65–70.
14. Hale SL, Lange R, Alker KJ, Kloner RA. Correlates of reperfusion ventricular fibrillation in dogs. Am J Cardiol 1984;53:1397–400.
15. Bolli R, Patel B. Factors that determine the occurrence of reperfusion arrhythmias. Am Heart J 1988;115:20–9.
16. Iwanaga K, Takano H, Ohtsuka M, et al. Effects of G-CSF on cardiac remodeling after acute myocardial infarction in swine. Biochem Biophys Res Commun 2004;325:1353–9.
17. Gabrilove JL, Jakubowski A, Fain K, et al. Phase I study of granulocyte colony-stimulating factor in patients with transitional cell carcinoma of the urothelium. J Clin Invest 1988; 82:1454–61.
18. Bensinger WI, Clift RA, Anasetti C, et al. Transplantation of allogeneic peripheral blood stem cells mobilized by recombinant human granulocyte colony stimulating factor. Stem Cells 1996;14:90–105.
19. Ince H, Petzsch M, Kleine HD, et al. Prevention of left ventricular remodeling with granulocyte colony-stimulating factor after acute myocardial infarction: final 1-year results of the Front-Integrated Revascularization and Stem Cell Liberation in Evolving Acute Myocardial Infarction by Granulocyte Colony-Stimulating Factor (FIRSTLINE-AMI) Trial. Circulation 2005;112:173–80.
20. Ince H, Petzsch M, Kleine HD, et al. Preservation from left ventricular remodeling by front-integrated revascularization and stem cell liberation in evolving acute myocardial infarction by use of granulocyte-colony-stimulating factor (FIRSTLINE-AMI). Circulation 2005;112:3097–106.
21. Avalos BR. Molecular analysis of the granulocyte colony-stimulating factor receptor. Blood 1996;88:761–77.

22. Tsang A, Hausenloy DJ, Mocanu MM, Yellon DM. Post-conditioning: a form of "modified reperfusion" protects the myocardium by activating the phosphatidylinositol 3-kinase-Akt pathway. Circ Res 2004;95:230–2.
23. Kang HJ, Kim HS, Zhang SY, et al. Effects of intracoronary infusion of peripheral blood stem-cells mobilised with granulocyte-colony stimulating factor on left ventricular systolic function and restenosis after coronary stenting in myocardial infarction: the MAGIC cell randomised clinical trial. Lancet 2004;363:751–6.
24. Weisbart RH, Golde DW, Clark SC, Wong GG, Gasson JC. Human granulocyte-macrophage colony-stimulating factor is a neutrophil activator. Nature 1985;314:361–3.
25. Barron HV, Cannon CP, Murphy SA, Braunwald E, Gibson CM. Association between white blood cell count, epicardial blood flow, myocardial perfusion, and clinical outcomes in the setting of acute myocardial infarction: a thrombolysis in myocardial infarction 10 substudy. Circulation 2000;102: 2329–34.
26. Adachi Y, Imagawa J, Suzuki Y, et al. G-CSF treatment increases side population cell infiltration after myocardial infarction in mice. J Mol Cell Cardiol 2004;36: 707–10.
27. Sugano Y, Anzai T, Yoshikawa T, et al. Granulocyte colony-stimulating factor attenuates early ventricular expansion after experimental myocardial infarction. Cardiovasc Res 2005;65:446–56.

The EMBO Journal (2006) 25, 2388–2396 | © 2006 European Molecular Biology Organization | All Rights Reserved 0261-4189/06
www.embojournal.org

THE EMBO JOURNAL

# Crystal structures of VAP1 reveal ADAMs' MDC domain architecture and its unique C-shaped scaffold

**Soichi Takeda[1,2,*], Tomoko Igarashi[1], Hidezo Mori[1] and Satohiko Araki[3]**

[1]Department of Cardiac Physiology, National Cardiovascular Center Research Institute, Suita, Osaka, Japan, [2]Laboratory for Structural Biochemistry, Riken Harima Institute at SPring-8, Mikazuki, Sayo, Hyogo, Japan and [3]Sugashima Marine Biological Laboratory, Graduate School of Science, Nagoya University, Toba, Mie, Japan

**ADAMs (a disintegrin and metalloproteinase) are sheddases possessing extracellular metalloproteinase/disintegrin/cysteine-rich (MDC) domains. ADAMs uniquely display both proteolytic and adhesive activities on the cell surface, however, most of their physiological targets and adhesion mechanisms remain unclear. Here for the first time, we reveal the ADAMs' MDC architecture and a potential target-binding site by solving crystal structures of VAP1, a snake venom homolog of mammalian ADAMs. The D-domain protrudes from the M-domain opposing the catalytic site and constituting a C-shaped arm with cores of $Ca^{2+}$ ions. The disintegrin-loop, supposed to interact with integrins, is packed by the C-domain and inaccessible for protein binding. Instead, the hyper-variable region (HVR) in the C-domain, which has a novel fold stabilized by the strictly conserved disulfide bridges, constitutes a potential protein–protein adhesive interface. The HVR is located at the distal end of the arm and faces toward the catalytic site. The C-shaped structure implies interplay between the ADAMs' proteolytic and adhesive domains and suggests a molecular mechanism for ADAMs' target recognition for shedding.**

*The EMBO Journal* (2006) 25, 2388–2396. doi:10.1038/sj.emboj.7601131; Published online 11 May 2006
*Subject Categories*: signal transduction; structural biology
*Keywords*: ADAM; MDC; protein–protein interaction shedding; snake venom metalloproteinase

## Introduction

ADAMs (a disintegrin and metalloproteinase) or MDC (metalloproteinase/disintegrin/cysteine-rich) proteins comprise an emerging class of mammalian metalloproteinases with potential regulatory roles in cell–cell and cell–matrix adhesion and signalling (Becherer and Blobel, 2003; Seals and Courtneidge, 2003; White, 2003; Blobel, 2005). To date, over 30 ADAMs have been identified in a variety of species from fission yeast to human. Roughly, half of these are believed to function as active metalloproteinases and thus to constitute major membrane-bound sheddase that can proteolytically release cell-surface-protein ectodomains including growth factors and cytokines, their receptors and cell adhesion molecules. For example, ADAM17 (TACE, TNF-α converting enzyme) releases many cell-surface proteins including TNF-α precursor (Black *et al*, 1997; Moss *et al*, 1997) and ADAM10 (kuzbanian), which dictates lateral inhibition of *Drosophila* neurogenesis (Rooke *et al*, 1996), releases Notch ligand Delta (Qi *et al*, 1999) and Notch itself (Pan and Rubin, 1997). With regard to cellular interactions, fertilin α and β (ADAM1 and ADAM2, respectively) have been identified as sperm surface molecules essential for fertilization (Primakoff *et al*, 1987; Blobel *et al*, 1990, 1992) and meltrin α (ADAM12) is implicated in myogenesis (Yagami-Hiromasa *et al*, 1995). ADAMs have been associated with numerous diseases including arthritis, Alzheimer's disease, and cancer (Duffy *et al*, 2003; Moss and Bartsch, 2004). ADAM33 has been genetically linked with asthma (Van Eerdewegh *et al*, 2002). ADAMs uniquely display both proteolytic and adhesive activities on the cell surface, however, most of their physiological targets and the adhesion mechanisms remain unclear.

Disintegrins are small proteins (40–90 aa) isolated from snake venom typically with an Arg-Gly-Asp (RGD) recognition sequence on an extended loop (disintegrin-loop) that inhibit platelet aggregation via integrin binding (Huang *et al*, 1987; Calvete *et al*, 2005). ADAMs are unique among cell surface proteins in possessing a disintegrin (D-) domain and thus it has been suggested that integrins might be common receptors for ADAMs (Blobel *et al*, 1992; Evans, 2001; White, 2003). However, the RGD sequence in the ADAMs' disintegrin-loop is usually replaced by XXCD and therefore, its adhesive potential has been controversial. Both the ADAMs' D- and cysteine-rich (C-) domains are involved in the protein–protein interactions (Myles *et al*, 1994; Almeida *et al*, 1995; Zolkiewska, 1999; Iba *et al*, 2000; Gaultier *et al*, 2002; Smith *et al*, 2002), however, the details of the interactions have remained elusive. This is because high-resolution structures have been available only for isolated domains (Maskos *et al*, 1998; Orth *et al*, 2004; Janes *et al*, 2005) and no structural information has been available for the C-domain of the canonical ADAMs. To clarify the molecular mechanisms of target recognition for shedding by and of cellular adhesion via ADAMs, elucidation of the atomic structure of the ADAMs' MDC domains is indispensable.

To obtain structural data on an ADAM family member, we exploited the fact that hemorrhagic P-III snake venom metalloproteinases (SVMPs) share the ADAMs' MDC architecture (Jia *et al*, 1996; Evans, 2001; Fox and Serrano, 2005). Most ADAMs possess additionally, EGF-like, transmembrane and cytoplasmic domains and therefore are primarily membrane-associated, whereas SVMPs are secreted. Vascular apoptosis-inducing protein-1 (VAP1) is a disulfide-bridged

*Corresponding author. Department of Cardiac Physiology, National Cardiovascular Center Research Institute, Fujishirodai 5-7-1, Suita, Osaka, 565-8565, Japan. Tel.: +81 6 6833 5012 ext.2381; Fax: +81 6 6872 7485; E-mail: stakeda@ri.ncvc.go.jp

Received: 17 February 2006; accepted: 12 April 2006; published online: 11 May 2006

homodimer P-III SVMP isolated from *Crotalus atrox* venom (Masuda *et al*, 1998, 2000). VAP1's stability and intrinsic two-fold symmetry enabled us to solve the crystal structures at 2.5-Å resolution. The structure reveals the residues that are important for stabilizing the MDC architecture are strictly conserved throughout the primary structure among all the known ADAMs. Therefore, the present structure represents the general architecture of ADAMs' MDC domains and provides insights into the molecular mechanism of the ADAMs' target recognition.

## Results

### *Structure determination*

VAP1 yielded crystals readily, and initial phases were determined by molecular replacement method using the structure of P-I SVMP, acutolysin-C (1QUA) (Zhu *et al*, 1999) as a starting model. Although the initial model, with 99 identical residues out of 197, represented less than 50% of the total molecule, two distinct local noncrystallographic two-fold symmetry (NCS) operations (see below) allowed us to completely model the whole molecule. The native structures were determined from the crystals with two distinct space groups, $P2_12_12_1$ and $P4_12_12$, both at 2.5-Å resolution (Table I). Orthorhombic crystals were used for inhibitor soaking and the GM6001 ((3-(*N*-hydroxycarboxamido)-2-isobutyl-propanoyl-Trp-methylamide))-bound structure was determined at 3.0-Å resolution (Table I). In either crystal forms, the asymmetric unit contained one dimer molecule. The four monomers in the two crystal forms have almost identical structures, except for slight variations in their domain orientations, terminal residues, surface loops and active-site GM6001-binding region.

### *MDC architecture*

The MDC architecture of VAP1 is shown in Figure 1A and B. The metalloproteinase (M-) domains in the dimer are related by NCS such that their active sites point in opposite directions and an intermolecular disulfide bridge is formed between symmetry-related Cys365 residues (Figure 1A). The M-domain is followed by a disintegrin (D-) domain that is further divided into $D_s$- and $D_a$-domains (see below). The $D_s$-domain protrudes from the M-domain close to the $Ca^{2+}$-binding site I (see below) opposing the catalytic site. The D-domain forms a C-shaped arm, together with the cysteine-rich (C-) domain, with its concave surface toward the M-domain. There are no direct interactions between the arm and the M-domain. Notably, the distal portion of the C-domain comes close to

Table I Data collection and refinement statistics

| | Native (orthorhombic) | Native (tetragonal) | GM6001-bound |
|---|---|---|---|
| *Data collection* | | | |
| Space group | $P2_12_12_1$ | $P4_12_12$ | $P2_12_12_1$ |
| *Cell dimensions* | | | |
| *a*, *b*, *c* (Å) | 86.7, 93.3, 137.7 | 93.9,93.9,244.8 | 86.3, 91.4, 136.0 |
| α, β, γ (deg) | 90, 90, 90 | 90, 90, 90 | 90, 90, 90 |
| Resolution (Å) | 50–2.50 (2.59–2.50) | 50–2.50 (2.59–2.50) | 50–2.95 (3.06–2.95) |
| $R_{merge}$[a] | 0.072 (0.369) | 0.084 (0.380) | 0.072 (0.367) |
| $I/\sigma I$ | 14.4 (2.9) | 18.7 (7.1) | 12.6 (4.3) |
| Completeness (%) | 99.4 (98.8) | 99.7 (99.6) | 99.9 (99.4) |
| Redundancy | 3.91 | 12.7 | 4.95 |
| *Refinement* | | | |
| Resolution (Å) | 50–2.50 (2.59–2.50) | 50–2.50 (2.59–2.50) | 50–2.95 (3.06–2.95) |
| No. of reflections | 38874 | 38786 | 23295 |
| $R_{work}$[b]/$R_{free}$[c] | 0.212/0.258 | 0.229/0.269 | 0.208/0.264 |
| *No. of atoms* | | | |
| Protein | 6558 | 6513 | 6558 |
| $Zn^{2+}$ | 2 | 2 | 2 |
| $Ca^{2+}$ | 4 | 4 | 4 |
| $Co^{3+}$ | 1 | | 1 |
| *N*-acetyl glucosamine | 56 | 42 | 56 |
| *GM6001* | | | 56 |
| Water | 205 | 165 | 35 |
| *B-factors* | | | |
| Protein | 44.9 | 51.2 | 55.4 |
| $Zn^{2+}$ | 40.9 | 41.6 | 46.4 |
| $Ca^{2+}$ | 43.5 | 52.4 | 49.3 |
| $Co^{3+}$ | 35.5 | | 56.8 |
| *N*-acetyl glucosamine | 69.8 | 65.1 | 75.8 |
| GM6001 | | | 78.6 |
| Water | 39.8 | 41.5 | 37.0 |
| *R.m.s deviations* | | | |
| Bond lengths (Å) | 0.0052 | 0.0080 | 0.0038 |
| Bond angles (deg) | 1.18 | 1.39 | 0.92 |

[a] $R_{merge} = \sum_{hkl}\sum_i |I_i(hkl) - \langle I(hlk)\rangle| / \sum_{hkl}\sum_i I_i(hkl)$, where $I_i(hkl)$ is the *i*th intensity measurement of reflection *hkl* and $\langle I(hlk)\rangle$ is its average.
[b] $R_{work} = \sum(||F_{obs}| - |F_{calc}||)/\sum|F_{obs}|$.
[c] $R_{free}$ = *R*-value for a randomly selected subset (5%) of the data that were not used for minimization of the crystallographic residual.
Highest resolution shell is shown in parenthesis.
For each data set, single crystal was used for measurement.

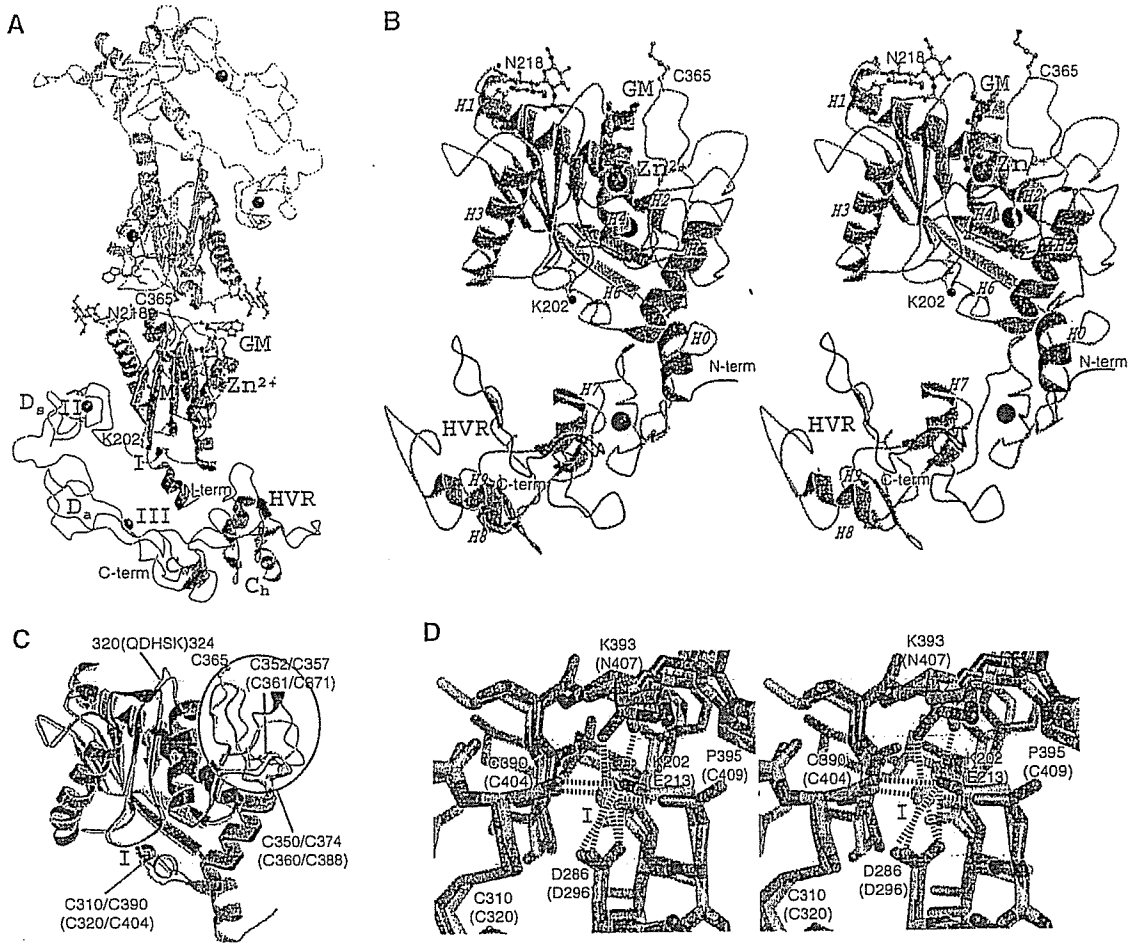


Figure 1 MDC architecture. (A) VAP1 dimer viewed from the NCS axis. The H0-helix, M-domain, linker, $D_s$-, $D_a$-, $C_w$-, and $C_h$-domains and HVRs belonging to the one monomer are shown in red, yellow, gray, cyan, pink, gray, green and blue, respectively. The disulfide-linked counterpart is shown in gray. Zinc and calcium ions are represented as red and black spheres, respectively. The NAG (*N*-acetyl-glucosamine, in orange) moieties linked to Asn218, the calcium-mimetic Lys202 and the bound inhibitor GM6001 (GM, in green) are in ball-stick representations. (B) Stereo view of VAP1 monomer from the direction nearly perpendicular to (A). The helix numbers are labelled. (C) Superposition of the M-domains of ADAM33 (blue) and VAP1 (yellow). The calcium ion bound to site I and the zinc ion in ADAM33 are represented by black and red spheres, respectively. The disulfide bridges are indicated in black and blue letters for VAP1 and ADAM33, respectively. The QDHSK sequence for the dimer interface in VAP1 (residues 320–324) is in red. (D) Comparison of the calcium-binding site I structures of ADAM33 (blue) and VAP1 (yellow) *in stereo*. The residues in ADAM33 and in VAP1 are labelled in blue and black, respectively. A calcium ion and a water molecule bound to ADAM33 are represented as green and red spheres, respectively. The ammonium group of Lys202 in VAP1 occupies the position of the calcium ion in ADAM33. In ADAM33 (Orth *et al*, 2004), side-chain oxygen atoms of Glu213, Asp296 and Asn407, the carbonyl oxygen of Cys404 and a water molecule form the corners of a pentagonal bipyramid and ligand to the calcium ion.

and faces toward the catalytic site in the M-domain. The C-terminus Tyr610 is located proximal to the boundary between the $D_a$- and C-domains (Figure 1A and B). Aside from Cys365, each monomer contains 34 cysteinyl residues, all of which are involved in disulfide bonding, and their spacings are strictly conserved among ADAMs (Figure 2 and Supplementary Figure 1) except within the substrate-binding (between the helices H4 and H5) and the HVR (see below) regions. Figure 2 provides a selected subset of the sequence alignments and the entire alignments of VAP1 and 39 ADAM sequences, including all 23 human ADAMs so far available, can be found as Supplementary Figure 1.

### *M-domain*

Each VAP1 M-domain corresponds to a very similar structure to that of ADAM33 (Orth *et al*, 2004), with a flat ellipsoidal shape having a central core made up of five stranded β-sheets and five α-helices and a conserved methionine (Met-turn) below the active site histidine residues, which bears the typical structural feature of metzincin family of metalloproteinases (Bode *et al*, 1993). However, they differ in the dimer interface and the loop structure around the substrate-binding site (Figure 1C) that corresponds to the variable region in the primary structure (between the helices H4 and H5, see Figure 2). The N-terminal helix (H0) is also unique in VAP1. The dimer interface is best characterized by the recognition sequence QDHSK (residues 320–324, see Figure 1C and Supplementary Figure 2A–C) and by Cys365, however these are not conserved among ADAMs; therefore, none of the ADAMs' M-domains are suggested to form a stable dimer as VAP1. A peptide-like hydroxamate inhibitor GM6001 binds to VAP1 (Figure 1A and B, and Supplementary Figure 2D and E) in exactly the same manner as in the marimastat-ADAM33 M-domain complex (Orth *et al*, 2004), suggesting that the catalytic sites of VAP1 and ADAM33 share a common substrate recognition mechanism. The ADAM33

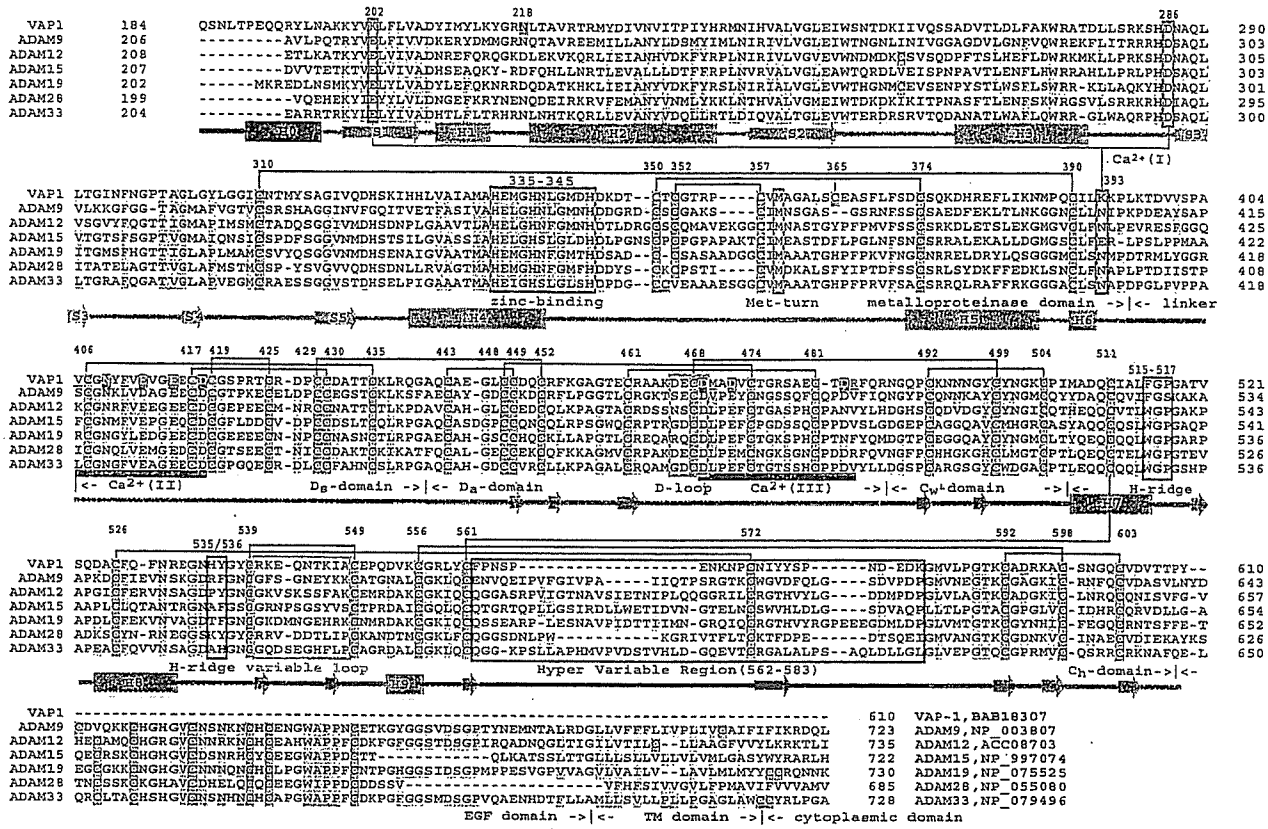


Figure 2 Sequence alignments of VAP1 and human ADAMs. The cysteinyl residues and the conserved residues are shaded in pink and yellow, respectively. Disulfide bridges, secondary structures and domains are drawn schematically. The HVR, calcium-binding site I, catalytic site and disintegrin-loop (D-loop) are boxed in blue, red, green and cyan, respectively. The hydrophobic ridges (H-ridges) are indicated. Calcium-binding sites II and III and the coordinating residues (shaded in red) are indicated. The NCBI accession numbers for the sequences are indicated.

M-domain structure suggests that most ADAMs have a $Ca^{2+}$-binding site (designated $Ca^{2+}$-binding site I) opposing the active-site cleft; however, in VAP1, the distal ammonium group of Lys202 substitutes for the $Ca^{2+}$ ion (Figure 1D). Replacement of the calcium-coordinating glutamate residue with lysine also occurs in ADAM16, ADAM25 and ADAMs38–40 (Supplementary Figure 1).

### *C-shaped arm*

The D-domain follows the M-domain, with a short linker that allows slightly variable domain orientations at V405 as a pivotal point (Figure 3C). The D-domain is further divided into two structural subdomains (Figure 3), the 'shoulder' ($D_s$-domain, residues 396–440) and the 'arm' ($D_a$-domain, residues 441–487). The $D_s$- and $D_a$-domains constitute a continuous C-shaped arm, together with the following N-terminus region of the C-domain which we designate the 'wrist' ($C_w$-domain, residues 488–505). There are three disulfide bonds in the $D_s$-domain, three in the $D_a$-domain and one in the $C_w$-domain. The subdomains are connected by single disulfide bridges (Figures 2 and 3A) with slightly variable angles (Figure 3B).

Both the $D_s$- and $D_a$-domains contain structural calcium-binding sites. In the $D_s$-domain, the side-chain oxygen atoms in residues Asn408, Glu412, Glu415 and Asp418, and the carbonyl oxygen atoms of Val405 and Phe410 are involved in pentagonal bipyramidal coordination and constitute $Ca^{2+}$-binding site II (Figures 2 and 3A). Notably, these residues are strictly conserved among all known ADAMs (Supplementary Figure 1). However, the side-chain oxygens of Asp469, Asp472 and Asp483, and carbonyl oxygens of Met470 and Arg484 form the corners of a pentagonal bipyramid to the calcium ligand and constitute the $D_a$-domain $Ca^{2+}$-binding site III (Figures 2 and 3A) and these residues are highly conserved among ADAMs except ADAM10 and ADAM17 (Supplementary Figure 1). Because of the few secondary-structural elements, bound calcium ions and the disulfide bridges are essential for the structural rigidity of ADAM's C-shaped arm. The RGD-containing disintegrin trimestatin (Fujii *et al*, 2003) has a similar structure with the $D_a$-domain (r.m.s.d of 1.24 Å, Figure 3B); however, no disintegrins have been shown to bind $Ca^{2+}$ ions.

Using isolated D-domains or portions thereof, numerous ADAMs and P-III SVMPs have been shown to interact specifically with particular integrins (Evans, 2001; White, 2003; Calvete *et al*, 2005). However, the disintegrin-loop is packed against the $C_w$-domain and a disulfide bridge (Cys468–Cys499) further stabilizes the continuous structure (Figure 3A). Therefore, the disintegrin-loop is inaccessible for protein binding.

### *Hand domain*

The 'hand' domain ($C_h$-domain, residues 505–610) follows the $C_w$-domain. The $C_h$-domain, together with the $C_w$-domain, constitutes a novel fold (Figure 4A). In either crystal form, VAP1 dimers interact with molecules of neighboring

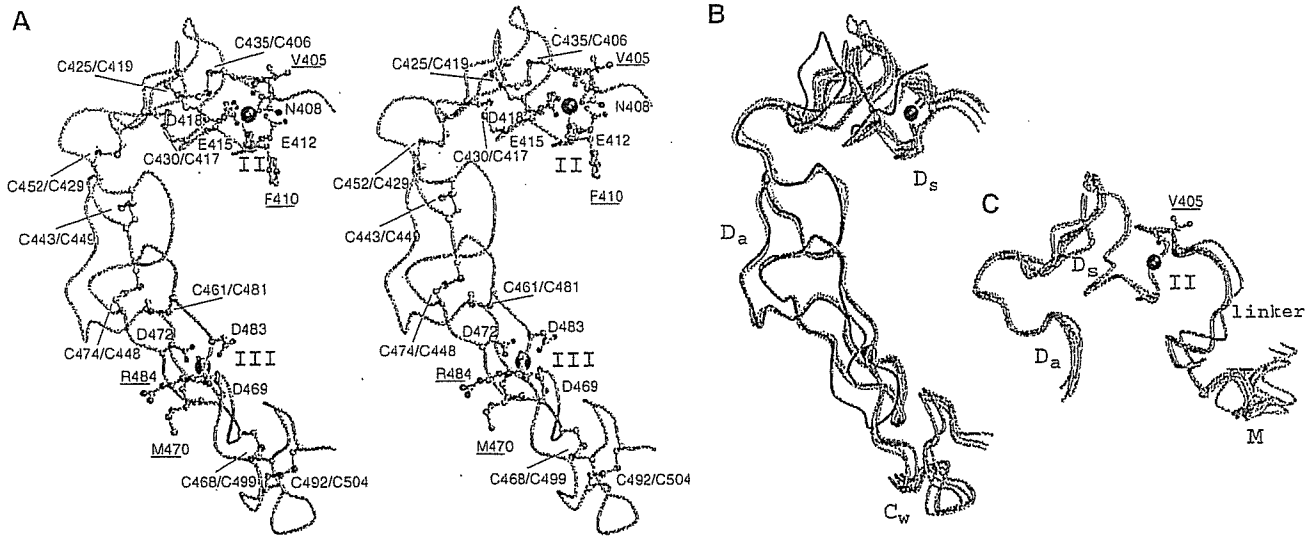


Figure 3 Arm structure. (A) Arm structure *in stereo*. The $D_s$-, $D_a$-, and $C_w$-domains are in cyan, pink and light green, respectively. The calcium-coordinating residues and the disulfide bridges are shown in red and green, respectively. The residues with carbonyl oxygen atoms involved in calcium coordination are underlined. Calcium ions are represented as black spheres. The disintegrin-loop (DECD) is in blue. (B) Superimposition of the four $D_a$-domains of VAP1 and trimestatin (1J2L). Trimestatin and its RGD loop are shown in red and blue, respectively. (C) Superimposition of the four $D_s$-domains. The linker between the M- and $D_s$-domains is shown in gray. Val405 at the pivotal point is indicated.

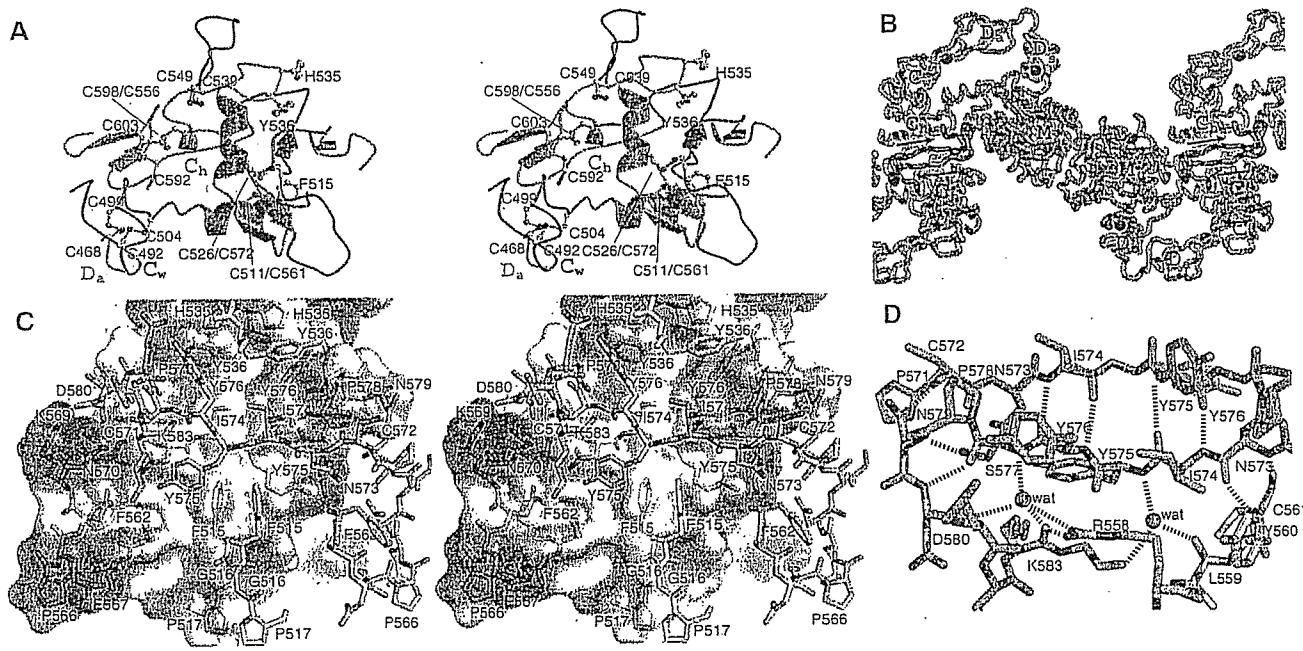


Figure 4 C-domain architecture and HVR. (A) The C-domain architecture *in stereo*. The $C_w$- and $C_h$-domains are in gray and light green, respectively. The disulfide bridges and the residues forming the hydrophobic ridges are indicated. The HVR and its NCS counterpart are shown in red and blue, respectively. The variable loop (residues 539–549), flanked by two adjacent cysteine residues, is in green. (B) Crystal packing in the orthorhombic crystal. The crystallographically equivalent molecules (HVRs) are in cyan (blue) and pink (red), respectively. The arrows indicate the directions of the HVR chains. Zinc and calcium ions are represented as red and black spheres, respectively. (C) Interactions between the HVRs (cyan and pink) *in stereo*. The molecular surface of the cyan molecule is shown with the electrochemical surface potential (red to blue). The residues constituting the hydrophobic ridges are in yellow. The residues are labelled in blue and red for cyan and pink, respectively. (D) Water-mediated hydrogen-bond network in the HVR. The HVR residues are in pink and cyan; non-HVR residues in the pink molecule are in gray.

units through the $C_h$-domains such that the molecules form a handshake (Figure 4B). Each $C_h$-domain interacts with its counterpart through a relatively large complementary surface of 860 Å$^2$ forming another NCS at the center, although VAP1 exists as dimers, not as oligomers, and is mono-dispersed in solution (data not shown).

### *HVR as a potential adhesive interface*

$C_h$-domain residues 562–583 are predominantly involved in the handshake (Figure 4B). This is the region in which the ADAM sequences are most divergent and variable in length (16–55 aa) (Figure 2 and Supplementary Figure 1). We have designated this as the hyper-variable region (HVR). The HVR

is subdivided into two structural elements. The N-terminal portion (residues 562–572) fits into an extended loop, filling the gap between the M-domain and the neighboring molecule's $C_h$-domain and thus fixing the position of the arm (Figure 4B). The variable structures and less-specific interactions suggest that this loop is stabilized by crystal packing. Some ADAMs possess a putative fusion peptide in this segment typical of viral fusion proteins (Blobel *et al*, 1992; Yagami-Hiromasa *et al*, 1995), although their role in the actual fusion process has not been demonstrated. However, the remainder of the HVR (residues 572–583) interacts extensively with its counterpart by forming an antiparallel β strand at the center (Figure 4C and D). Although the ability to form β strand is predictable from the sequence, this β strand is stabilized mainly by interchain interactions (Figure 4D). There are no intrachain hydrogen bonds between residues 574–577 and the remainder of the $C_h$-domain; however a water-mediated hydrogen-bond network stabilizes this segment (Figure 4D). Therefore, it appears, that this β strand might be formed by the induced-fit mechanism upon the association of the $C_h$-domains and that the conserved disulfide bond (Cys526–Cys572, see Figure 4D) may stabilize the structure when the HVRs are isolated in solution. In addition to the main-chain hydrogen bonds, side-chain atoms (particularly residues I574, Y575, Y576 and P578) in the HVR β strand contribute numerous von der Waals interactions with their counterparts. Aside from the HVR, aromatic residues located at both sides of the β strand in close proximity to the NCS axis create additional interaction surfaces: residues Phe515, Gly516, His535 and Tyr536 in the loop regions form hydrophobic ridges that fit complementarily into the NCS region (Figure 4C). The hydrophobic ridges are highly conserved among ADAMs (Figure 2 and Supplementary Figure 1), thus, in part, they may also constitute binding surfaces.

## Discussion

The VAP1 structures reveal highly conserved structural calcium-binding sites and the numbers and the spacings of cysteinyl residues that are essential for maintaining structural rigidity and spatial arrangement of the ADAMs' MDC domains. The C-shaped MDC architecture implies meaningful interplay between the domains and their potential roles in physiological functions.

The HVR creates a novel interaction interface in collaboration with the conserved hydrophobic ridges. Different ADAMs have distinct HVR sequences, which result in distinct surface features, thus, they may function in specifying binding proteins. The HVR is at the distal end of the C-shaped arm and points toward the M-domain catalytic site, with a distance of ~4 nm in between them. Collectively, these observations suggest that the HVR captures the target or associated protein that is processed by the catalytic site (Figure 5). The disintegrin portion is located opposit to and apart from the catalytic site and, thus, might play a primary role as a scaffold that allocates these two functional units spatially. The C-shaped structure also implies how the ADAMs' C-domains cooperate with their M-domains (Reddy *et al*, 2000; Smith *et al*, 2002). In membrane-bound ADAMs, the EGF-like domain (~60 aa) follows the $C_h$-domain (Figure 2) and presumably works as a rigid spacer connecting the MDC-domains with and orientating against the membrane-spanning region (Figure 5A). Many ADAMs are proteolytically inactive (because of the defects in the catalytic HEXXHXXGXXHD sequence or the post-translational removal of the M-domain), and several of these are important developmentally. Therefore, the HVR may also work to modulate cell–cell and cell–matrix interactions. There is some experimental evidence for C-domain-mediated adhesion. Peptides encompassing the HVR and the hydrophobic ridge from P-III SVMPs interfere with platelet interaction and collagen binding (Kamiguti *et al*, 2003). A recombinant atrolysin-A C-domain specifically binds collagen I and von Willebrand factor (vWF) and blocks collagen–vWF interaction (Jia *et al*, 2000; Serrano *et al*, 2005). ADAM12 interacts with cell-surface syndecan through its C-domain and mediates integrin-dependent cell spreading (Iba *et al*, 2000). The D/C-domain portion of ADAM13 binds to the ECM proteins laminin and fibronectin (Gaultier *et al*, 2002). However, most of these studies do not assign specific regions of the C-domain to these interactions and the molecular recognition mechanisms are to be elucidated.

ADAM10 and ADAM17 lack the $Ca^{2+}$-binding site III and show less sequence similarities in the C-domain with other

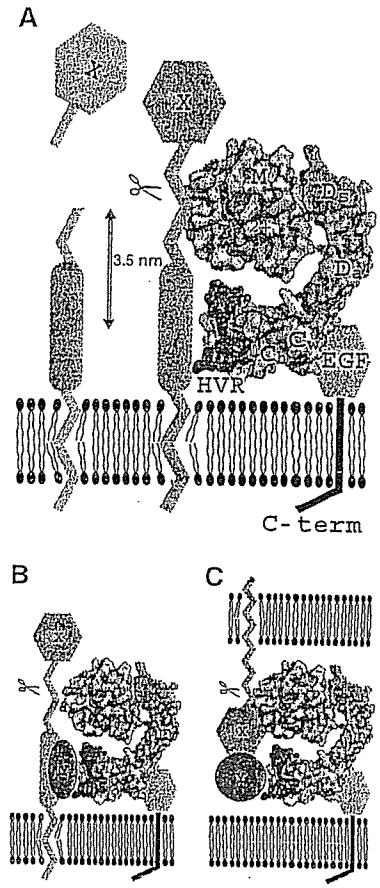


**Figure 5** Models for ADAM's shedding. The molecular surface of the VAP1 monomer, without VAP1's unique H0-helix, are colored as in Figure 1A. Hydrophobic ridges are in yellow. EGF-like, transmembrane and cytoplasmic domains are represented schematically. (A) Membrane-anchored substrate molecule 'X' is directly recognized and captured by the HVR on the membrane-bound ADAM molecule. The distance between the center of the HVR (Tyr575) and the catalytic zinc ion is about 3.5 nm. (B) Substrate 'X' is recognized by the ADAM HVR via binding with an associated protein 'Y'. (C) ADAM cleaves substrate 'X' in *trans* via binding with an associated protein 'Y'.

canonical ADAMs (Supplementary Figure 1). Comparison of the recently solved ADAM10 D/C-domain partial structure ($ADAM10_{D+C}$) (Janes *et al*, 2005) and that of VAP1 reveals that the atypical ADAM10 shares the continuous $D_a/C_w$ structure and the $C_h$-domain scaffold with VAP1; however, it has an disordered $D_s$-domain and an alternate HVR structure and a different orientation between $C_w$- and $C_h$-domains (Figure 6). The locations of four of the five disulfide bridges within the $C_h$-domain are conserved between VAP1 and ADAM10 (Figure 6B and C) and thus, they enabled us to align the two sequences (Figure 6E). Based on this alignment, we completed entire alignments (Supplementary Figure 1) including 38 sequences of mammalian ADAMs and *Schizosaccharomyces pombe* Mde10 (Nakamura *et al*, 2004), presumably the founding member of the ADAM family in evolutionary terms. The $ADAM10_{D+C}$ structure lacks the eight residues (583–590 in ADAM10) that may form a flexible loop. However, VAP1 (Figure 6E) and the canonical ADAMs except for ADAM8 (Supplementary Figure 1) have extra 16 residues in this segment that, in part, forms a variable loop, flanked by the adjacent cysteinyl residues (Cys539 and Cys549 in VAP1) and protrudes from the main body of the C-domain (Figures 4A and 6B). The variable loop has highest temperature factor in the molecule and resembles to the disintegrin-loop, thus can be an additional protein-binding interface. The six VAP1 monomer molecules represent almost the same $C_w/C_h$ domain orientation (data not shown), however that is distinct from that of ADAM10 (Figure 5A). Thus, the possibility whether different ADAMs have distinct $C_w/C_h$ domain orientation remains to be established. Janes *et al* (2005) have shown that the three glutamate residues outside of HVR are essential for ADAM10-mediated ephrin proteolysis in *trans*, however, roles of the ADAM10 HVR has not been examined. An extensive molecular surface of the elongated arm structure (12 000 $Å^2$ for the VAP1 D/C-domains) might reveal additional protein–protein interaction interfaces other than the HVR. Multiple charged residues in the D-domain are essential for ADAM28 binding to $\alpha4\beta1$ (Bridges *et al*, 2003) and the $RX_6DLPEF$ motif has been proposed for integrin $\alpha9\beta1$ binding (Eto *et al*, 2002). However, the D-domain portion of the C-shaped scaffold is away from the catalytic site; thus, those additional sites might not directly serve as target recognition interfaces for catalysis.

Uniquely among cell-surface proteins, ADAMs display both proteolytic and adhesive activities. The VAP1 structure reveals that these functions are spatially allocated to the ends of the unique C-shaped scaffold and face each other. This spatial allocation of the functional sites provide us insights

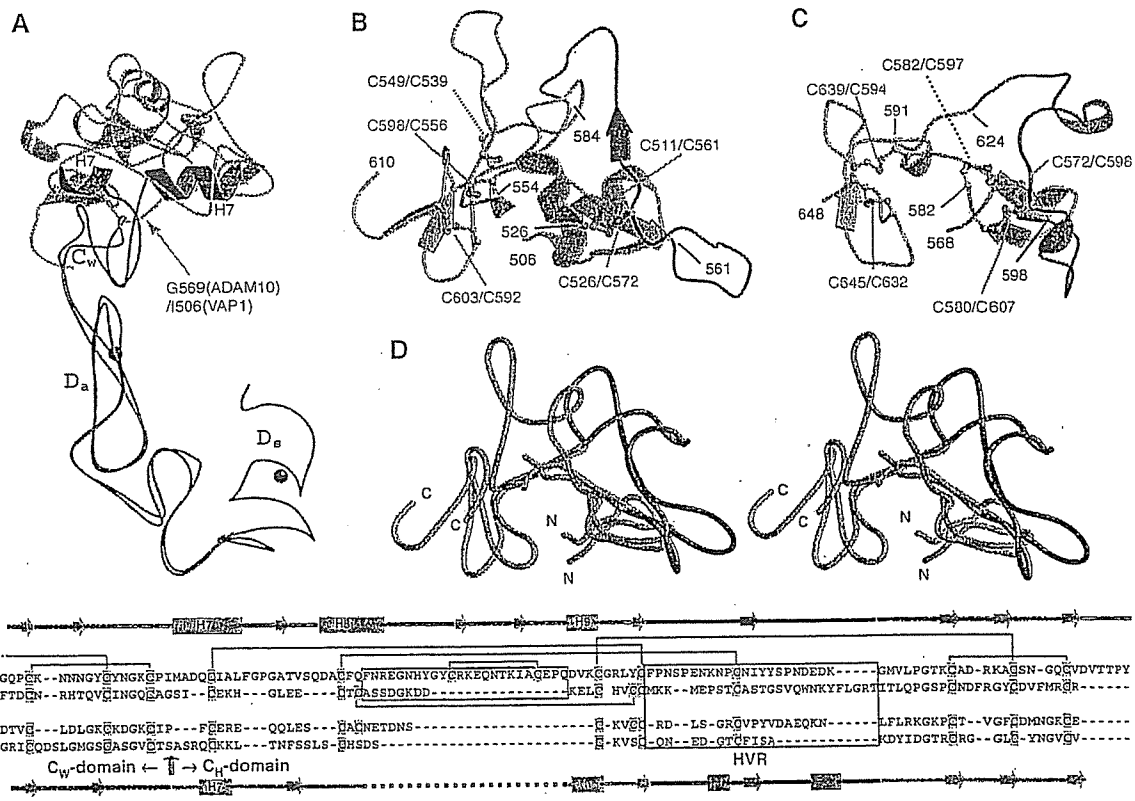


Figure 6 Comparison of the VAP1 and ADAM10 D/C domains. (A) Superimposition of the $D_a$-domains of ADAM10 and VAP1. The $D_s/D_a/C_w$-domains and the H7 helix of VAP1 and those of ADAM10 are shown in blue and red, respectively. The $C_h$-domains of VAP1 and ADAM10 are shown in cyan and pink, respectively. The arrow indicates the pivotal point between the $C_w$- and $C_h$-domains. Bound $Ca^{2+}$ ions in VAP1 are shown as black spheres. (B) Ribbon representation of the $C_h$-domain of VAP1. The HVR is shown in blue. The common scaffold between the VAP1 and ADAM10 $C_h$-domains are shown in cyan and the segment lacking in ADAM10 is shown in light green. Disulfide bridges are indicated. (C) Ribbon representation of the $C_h$-domain of ADAM10. The HVR is shown in red. Disulfide brides are indicated. (D) Superimposition of the $C_h$-domains of VAP1 and ADAM10 *in stereo* with the colors as in (B, C). The N- and C-termini of the $C_h$-domains are indicated. (E) Structure-based alignments of VAP1, bovine ADAM10 (cADAM10), human ADAM17 (hADAM17) and *S. pombe* Mde10 (Mde10) $C_w/C_h$-domains. Secondary structures and the disulfide bridges are represented schematically. The HVR sequences and the missing segment in the ADAM10 structure are boxed in blue and green, respectively.

into the molecular mechanism of ADAMs' target recognition, which ADAMs shed which key substrates in specific biological events. Since ADAMs are potential therapeutic targets, the distinct surface feature created by the HVR of the individual ADAMs might also provide insights into the future design of drugs with higher specificity for each member of ADAMs. We suggest that the HVR, not the disintegrin domain, should be the focus of searches for physiological targets of ADAMs.

## Materials and methods

### *Protein preparation and crystallization*

The details of the preparation, crystallization and preliminary X-ray analysis of VAP1 will be described elsewhere (T Igarashi *et al*, in preparation). VAP1 was isolated from the crude snake *Crotalus atrox* venom (Sigma-Aldrich, USA) and subjected to sitting- or hanging-drop vapor diffusion crystallization. Two distinct crystal forms ($P2_12_12_1$ and $P4_12_12$) were obtained with the reservoir solution containing 15% polyethyleneglycol 8000 and 100 mM sodium cacodylate at pH 6.5, with (orthorhombic form) or without (tetragonal form) 20 mM cobaltous chloride hexahydrate. GM6001-bound crystals were prepared by adding GM6001 (CALBIOCHEM) to the drop with the orthorhombic crystal at a final concentration qof 0.33 mM (twice the protein concentration) followed by a 12-h incubation. Crystals were flash-frozen under the nitrogen flow at 90 K.

### *Diffraction data collection*

All the diffraction data were collected at SPring-8 beamlines using either ADSC quantum 310R CCD (for the inhibitor-bound crystal at the beamline BL41XU with $\lambda = 1$ Å), Rigaku *R*-axis V imaging plate (for orthorhombic native crystal at the beamline BL45PX with $\lambda = 1$ Å) or Jupitor CCD (for the tetragonal crystal at the beamline BL45PX with $\lambda = 0.98$ Å) detectors at 90 K. The images were reduced using HKL2000. Both orthorhombic and tetragonal native data sets were collected to 2.5-Å resolution and inhibitor-bound crystal data sets were collected to 3.0 Å resolution (Table I).

### *Structural analysis*

All structures were solved by the molecular replacement method by MOLREP in the CCP4 suite (CCP4, 1994) by using acutolysin-C (1QUA) (Zhu *et al*, 1999) as a starting model. Initially, the MR solution obtained from the orthorhombic crystal data set, assumed two M-domains in the asymmetric units. After manual rebuilding by TURBO-FRODO, the model was subjected to tortional molecular dynamic refinements with restrained NCS averaging of the M-domains using CNS (Brunger *et al*, 1998) and iterative refinements and manual rebuilding of the model improved the electron-density map and enabled us to extend the model. First, we found the electron densities associated with the pieces of helical segments of the molecules and modelled them as poly-alanine chains. After cycles of refinements, we assigned those segments as the parts of helices H7 and H8, where the secondary structures are predicted to be helices, judging from the electron densities associated with the side chains. At this stage, four tyrosine residues, Tyr575 and Try576 within the central β strands of the HVRs were clearly defined, and we noticed that there was another NCS-axis between the C-domains. After iterative rounds of refinements with restrained NCS averaging of the C-domains and manual model building, we completed modelling of the C-domains. From this stage onward, no NCS averaging was included in the refinements. Next, we modelled the D-domains with the help of automated chain tracing using the program ARP/wARP (Perrakis *et al*, 1999) and with the structural model of trimestatin (1J2L) as a guide. After completely modelling the polypeptide chains, we noticed that isolated lobes of high electron densities surrounded by oxygen atoms occurred both in the $D_s$- and $D_a$-domains. For these sites, calcium ions fit optimally to the electron density with a refined occupancy of 100% and reasonably low *B*-values, thus, we included calcium ions in the model. We also assigned a cobalt ion, which was supplemented in the crystallization buffer for the orthorhombic crystal form, located between the M- and $D_s$-domains in the A molecule. The part of the carbohydrate chain linked to residue Asn218 (two *N*-acetylglocosamine (NAG) moieties) was modelled. Then, water molecules were assigned. The *VAP1* cDNA encodes a protein with 610 amino-acid residues; however, the N-terminus is processed by post-translational modification (Masuda *et al*, 1998, 2000). Here, protein sequencing of the de-blocked VAP1 molecule clarified that the Glu184 side chain was modified into a pyro-form. The electron densities associated with almost the entire molecule except for the first pyroglutamic acid were defined in either monomer within the orthorhombic crystal. In the final model, 86.1% of the residues lay in the most favorable region, 13.3% in the additionally allowed region and 0.7% in the generously allowed region of the Ramachandran plot. The tetragonal crystal and inhibitor-bound crystal were solved by MR with the domains of the refined orthorhombic apo-form as a starting model. In the final model, 83.6% (80.6%) of the residues lay in the most favorable region, 15.7% (18.9%) in the additionally allowed region and 0.7% (0.5%) in the generously allowed region for tetragonal (inhibitor-bound) crystals in the Ramachandran plot. In either crystal form, the asymmetric unit contained one dimer molecule. All six monomers had almost identical structures. Refinement statistics are shown in Table I.

### *PDB accession codes*

Atomic coordinates and structure factors have been deposited in the Protein Data Bank under accession codes 2ERO, 2ERP and 2ERQ for the orthorhombic native, GM6001-bound form and tetragonal-form, respectively.

### *Supplementary data*

Supplementary data are available at *The EMBO Journal* Online.

## Acknowledgements

We thank Yuko Oishi and staff in SPring-8 beamlines for assistance with data acquisition and Junichi Takagi for discussions and critical reading of the manuscript. This work was partly supported by Grant nano-001 for Research on Advanced Medical Technology from the Ministry of Health, Labor, and Welfare of Japan, and by grants from the Takeda Science Foundation, from the Kao Foundation for Arts and Science and from Senri Life Science Foundation. The authors declare no competing financial interests.

## References

Almeida EA, Huovila AP, Sutherland AE, Stephens LE, Calarco PG, Shaw LM, Mercurio AM, Sonnenberg A, Primakoff P, Myles DG, White JM (1995) Mouse egg integrin alpha 6 beta 1 functions as a sperm receptor. *Cell* 81: 1095–1104

Becherer JD, Blobel CP (2003) Biochemical properties and functions of membrane-anchored metalloprotease-disintegrin proteins (ADAMs). *Curr Top Dev Biol* 54: 101–123

Black RA, Rauch CT, Kozlosky CJ, Peschon JJ, Slack JL, Wolfson MF, Castner BJ, Stocking KL, Reddy P, Srinivasan S, Nelson N, Boiani N, Schooley KA, Gerhart M, Davis R, Fitzner JN, Johnson RS, Paxton RJ, March CJ, Cerretti DP (1997) A metalloproteinase disintegrin that releases tumour-necrosis factor-alpha from cells. *Nature* 385: 729–733

Blobel CP (2005) ADAMs: key components in EGFR signalling and development. *Nat Rev Mol Cell Biol* 6: 32–43

Blobel CP, Myles DG, Primakoff P, White JM (1990) Proteolytic processing of a protein involved in sperm-egg fusion correlates with acquisition of fertilization competence. *J Cell Biol* 111: 69–78

Blobel CP, Wolfsberg TG, Turck CW, Myles DG, Primakoff P, White JM (1992) A potential fusion peptide and an integrin ligand domain in a protein active in sperm-egg fusion. *Nature* 356: 248–252

Bode W, Gomis-Ruth FX, Stockler W (1993) Astacins, serralysins, snake venom and matrix metalloproteinases exhibit identical zinc-binding environments (HEXXHXXGXXH and Met-turn) and

topologies and should be grouped into a common family, the 'metzincins'. *FEBS Lett* 331: 134–140

Bridges LC, Hanson KR, Tani PH, Mather T, Bowditch RD (2003) Integrin alpha4beta1-dependent adhesion to ADAM 28 (MDC-L) requires an extended surface of the disintegrin domain. *Biochemistry* 42: 3734–3741

Brunger AT, Adams PD, Clore GM, DeLano WL, Gros P, Grosse-Kunstleve RW, Jiang JS, Kuszewski J, Nilges M, Pannu NS, Read RJ, Rice LM, Simonson T, Warren GL (1998) Crystallography & NMR system: a new software suite for macromolecular structure determination. *Acta Crystallogr D* 54 (Part 5): 905–921

Calvete JJ, Marcinkiewicz C, Monleon D, Esteve V, Celda B, Juarez P, Sanz L (2005) Snake venom disintegrins: evolution of structure and function. *Toxicon* 45: 1063–1074

CCP4 (1994) The CCP4 suite: programs for protein crystallography. *Acta Crystallogr D* 50: 760–763

Duffy MJ, Lynn DJ, Lloyd AT, O'Shea CM (2003) The ADAMs family of proteins: from basic studies to potential clinical applications. *Thromb Haemost* 89: 622–631

Eto K, Huet C, Tarui T, Kupriyanov S, Liu HZ, Puzon-McLaughlin W, Zhang XP, Sheppard D, Engvall E, Takada Y (2002) Functional classification of ADAMs based on a conserved motif for binding to integrin alpha 9beta 1: implications for sperm-egg binding and other cell interactions. *J Biol Chem* 277: 17804–17810

Evans JP (2001) Fertilin beta and other ADAMs as integrin ligands: insights into cell adhesion and fertilization. *BioEssays* 23: 628–639

Fox JW, Serrano SM (2005) Structural considerations of the snake venom metalloproteinases, key members of the M12 reprolysin family of metalloproteinases. *Toxicon* 45: 969–985

Fujii Y, Okuda D, Fujimoto Z, Horii K, Morita T, Mizuno H (2003) Crystal structure of trimestatin, a disintegrin containing a cell adhesion recognition motif RGD. *J Mol Biol* 332: 1115–1122

Gaultier A, Cousin H, Darribere T, Alfandari D (2002) ADAM13 disintegrin and cysteine-rich domains bind to the second heparin-binding domain of fibronectin. *J Biol Chem* 277: 23336–23344

Huang TF, Holt JC, Lukasiewicz H, Niewiarowski S (1987) Trigramin. A low molecular weight peptide inhibiting fibrinogen interaction with platelet receptors expressed on glycoprotein IIb–IIIa complex. *J Biol Chem* 262: 16157–16163

Iba K, Albrechtsen R, Gilpin B, Frohlich C, Loechel F, Zolkiewska A, Ishiguro K, Kojima T, Liu W, Langford JK, Sanderson RD, Brakebusch C, Fassler R, Wewer UM (2000) The cysteine-rich domain of human ADAM 12 supports cell adhesion through syndecans and triggers signaling events that lead to beta1 integrin-dependent cell spreading. *J Cell Biol* 149: 1143–1156

Janes PW, Saha N, Barton WA, Kolev MV, Wimmer-Kleikamp SH, Nievergall E, Blobel CP, Himanen JP, Lackmann M, Nikolov DB (2005) Adam meets Eph: an ADAM substrate recognition module acts as a molecular SWITCH for Ephrin cleavage *in trans*. *Cell* 123: 291–304

Jia LG, Shimokawa K, Bjarnason JB, Fox JW (1996) Snake venom metalloproteinases: structure, function and relationship to the ADAMs family of proteins. *Toxicon* 34: 1269–1276

Jia LG, Wang XM, Shannon JD, Bjarnason JB, Fox JW (2000) Inhibition of platelet aggregation by the recombinant cysteine-rich domain of the hemorrhagic snake venom metalloproteinase, atrolysin A. *Arch Biochem Biophys* 373: 281–286

Kamiguti AS, Gallagher P, Marcinkiewicz C, Theakston RD, Zuzel M, Fox JW (2003) Identification of sites in the cysteine-rich domain of the class P-III snake venom metalloproteinases responsible for inhibition of platelet function. *FEBS Lett* 549: 129–134

Maskos K, Fernandez-Catalan C, Huber R, Bourenkov GP, Bartunik H, Ellestad GA, Reddy P, Wolfson MF, Rauch CT, Castner BJ, Davis R, Clarke HR, Petersen M, Fitzner JN, Cerretti DP, March CJ, Paxton RJ, Black RA, Bode W (1998) Crystal structure of the catalytic domain of human tumor necrosis factor-alpha-converting enzyme. *Proc Natl Acad Sci USA* 95: 3408–3412

Masuda S, Hayashi H, Araki S (1998) Two vascular apoptosis-inducing proteins from snake venom are members of the metalloprotease/disintegrin family. *Eur J Biochem* 253: 36–41

Masuda S, Ohta T, Kaji K, Fox JW, Hayashi H, Araki S (2000) cDNA cloning and characterization of vascular apoptosis-inducing protein 1. *Biochem Biophys Res Commun* 278: 197–204

Moss ML, Bartsch JW (2004) Therapeutic benefits from targeting of ADAM family members. *Biochemistry* 43: 7227–7235

Moss ML, Jin SL, Milla ME, Bickett DM, Burkhart W, Carter HL, Chen WJ, Clay WC, Didsbury JR, Hassler D, Hoffman CR, Kost TA, Lambert MH, Leesnitzer MA, McCauley P, McGeehan G, Mitchell J, Moyer M, Pahel G, Rocque W, Overton LK, Schoenen F, Seaton T, Su JL, Warner J, Willard D, Becherer JD (1997) Cloning of a disintegrin metalloproteinase that processes precursor tumour-necrosis factor-alpha. *Nature* 385: 733–736

Myles DG, Kimmel LH, Blobel CP, White JM, Primakoff P (1994) Identification of a binding site in the disintegrin domain of fertilin required for sperm-egg fusion. *Proc Natl Acad Sci USA* 91: 4195–4198

Nakamura T, Abe H, Hirata A, Shimoda C (2004) ADAM family protein Mde10 is essential for development of spore envelopes in the fission yeast *Schizosaccharomyces pombe*. *Eukaryot Cell* 3: 27–39

Orth P, Reichert P, Wang W, Prosise WW, Yarosh-Tomaine T, Hammond G, Ingram RN, Xiao L, Mirza UA, Zou J, Strickland C, Taremi SS, Le HV, Madison V (2004) Crystal structure of the catalytic domain of human ADAM33. *J Mol Biol* 335: 129–137

Pan D, Rubin GM (1997) Kuzbanian controls proteolytic processing of Notch and mediates lateral inhibition during *Drosophila* and vertebrate neurogenesis. *Cell* 90: 271–280

Perrakis A, Morris R, Lamzin VS (1999) Automated protein model building combined with iterative structure refinement. *Nat Struct Biol* 6: 458–463

Primakoff P, Hyatt H, Tredick-Kline J (1987) Identification and purification of a sperm surface protein with a potential role in sperm-egg membrane fusion. *J Cell Biol* 104: 141–149

Qi H, Rand MD, Wu X, Sestan N, Wang W, Rakic P, Xu T, Artavanis-Tsakonas S (1999) Processing of the notch ligand delta by the metalloprotease Kuzbanian. *Science* 283: 91–94

Reddy P, Slack JL, Davis R, Cerretti DP, Kozlosky CJ, Blanton RA, Shows D, Peschon JJ, Black RA (2000) Functional analysis of the domain structure of tumor necrosis factor-alpha converting enzyme. *J Biol Chem* 275: 14608–14614

Rooke J, Pan D, Xu T, Rubin GM (1996) KUZ, a conserved metalloprotease-disintegrin protein with two roles in *Drosophila* neurogenesis. *Science* 273: 1227–1231

Seals DF, Courtneidge SA (2003) The ADAMs family of metalloproteases: multidomain proteins with multiple functions. *Genes Dev* 17: 7–30

Serrano SM, Jia LG, Wang D, Shannon JD, Fox JW (2005) Function of the cysteine-rich domain of the haemorrhagic metalloproteinase atrolysin A: targeting adhesion proteins collagen I and von Willebrand factor. *Biochem J* 391: 69–76

Smith KM, Gaultier A, Cousin H, Alfandari D, White JM, DeSimone DW (2002) The cysteine-rich domain regulates ADAM protease function *in vivo*. *J Cell Biol* 159: 893–902

Van Eerdewegh P, Little RD, Dupuis J, Del Mastro RG, Falls K, Simon J, Torrey D, Pandit S, McKenny J, Braunschweiger K, Walsh A, Liu Z, Hayward B, Folz C, Manning SP, Bawa A, Saracino L, Thackston M, Benchekroun Y, Capparell N, Wang M, Adair R, Feng Y, Dubois J, FitzGerald MG, Huang H, Gibson R, Allen KM, Pedan A, Danzig MR, Umland SP, Egan RW, Cuss FM, Rorke S, Clough JB, Holloway JW, Holgate ST, Keith TP (2002) Association of the ADAM33 gene with asthma and bronchial hyperresponsiveness. *Nature* 418: 426–430

White JM (2003) ADAMs: modulators of cell–cell and cell–matrix interactions. *Curr Opin Cell Biol* 15: 598–606

Yagami-Hiromasa T, Sato T, Kurisaki T, Kamijo K, Nabeshima Y, Fujisawa-Sehara A (1995) A metalloprotease-disintegrin participating in myoblast fusion. *Nature* 377: 652–656

Zhu X, Teng M, Niu L (1999) Structure of acutolysin-C, a haemorrhagic toxin from the venom of Agkistrodon acutus, providing further evidence for the mechanism of the pH-dependent proteolytic reaction of zinc metalloproteinases. *Acta Crystallogr D* 55: 1834–1841

Zolkiewska A (1999) Disintegrin-like/cysteine-rich region of ADAM 12 is an active cell adhesion domain. *Exp Cell Res* 252: 423–431

*Am J Physiol Heart Circ Physiol* 291: H1138–H1146, 2006.
First published April 28, 2006; doi:10.1152/ajpheart.00187.2006.

# Cardioprotective role of endogenous hydrogen peroxide during ischemia-reperfusion injury in canine coronary microcirculation in vivo

Toyotaka Yada,[1] Hiroaki Shimokawa,[3] Osamu Hiramatsu,[1] Yoshisuke Haruna,[2] Yoshitaka Morita,[2] Naoki Kashihara,[2] Yoshiro Shinozaki,[4] Hidezo Mori,[5] Masami Goto,[1] Yasuo Ogasawara,[1] and Fumihiko Kajiya[1]

[1]*Department of Medical Engineering and Systems Cardiology and* [2]*Division of Nephrology and Rheumatology, Department of Internal Medicine, Kawasaki Medical School, Kurashiki;* [3]*Department of Cardiovascular Medicine, Tohoku University Graduate School of Medicine, Sendai;* [4]*Department of Physiology, Tokai University School of Medicine, Isehara; and* [5]*Department of Cardiac Physiology, National Cardiovascular Center Research Institute, Suita, Japan*

Submitted 22 February 2006; accepted in final form 18 April 2006

**Yada, Toyotaka, Hiroaki Shimokawa, Osamu Hiramatsu, Yoshisuke Haruna, Yoshitaka Morita, Naoki Kashihara, Yoshiro Shinozaki, Hidezo Mori, Masami Goto, Yasuo Ogasawara, and Fumihiko Kajiya.** Cardioprotective role of endogenous hydrogen peroxide during ischemia-reperfusion injury in canine coronary microcirculation in vivo. *Am J Physiol Heart Circ Physiol* 291: H1138–H1146, 2006. First published April 28, 2006; doi:10.1152/ajpheart.00187.2006.—We have recently demonstrated that endogenous $H_2O_2$ plays an important role in coronary autoregulation in vivo. However, the role of $H_2O_2$ during coronary ischemia-reperfusion (I/R) injury remains to be examined. In this study, we examined whether endogenous $H_2O_2$ also plays a protective role in coronary I/R injury in dogs in vivo. Canine subepicardial small coronary arteries (≥100 μm) and arterioles (<100 μm) were continuously observed by an intravital microscope during coronary I/R (90/60 min) under cyclooxygenase blockade ($n$ = 50). Coronary vascular responses to endothelium-dependent vasodilators (ACh) were examined before and after I/R under the following seven conditions: control, nitric oxide (NO) synthase (NOS) inhibitor $N^G$-monomethyl-L-arginine (L-NMMA), catalase (a decomposer of $H_2O_2$), 8-sulfophenyltheophylline (8-SPT, an adenosine receptor blocker), L-NMMA + catalase, L-NMMA + tetraethylammonium (TEA, an inhibitor of large-conductance $Ca^{2+}$-sensitive potassium channels), and L-NMMA + catalase + 8-SPT. Coronary I/R significantly impaired the coronary vasodilatation to ACh in both sized arteries (both $P < 0.01$); L-NMMA reduced the small arterial vasodilatation (both $P < 0.01$), whereas it increased ($P < 0.05$) the ACh-induced coronary arteriolar vasodilatation associated with fluorescent $H_2O_2$ production after I/R. Catalase increased the small arterial vasodilatation ($P < 0.01$) associated with fluorescent NO production and increased endothelial NOS expression, whereas it decreased the arteriolar response after I/R ($P < 0.01$). L-NMMA + catalase, L-NMMA + TEA, or L-NMMA + catalase + 8-SPT further decreased the coronary vasodilatation in both sized arteries (both, $P < 0.01$). L-NMMA + catalase, L-NMMA + TEA, and L-NMMA + catalase + 8-SPT significantly increased myocardial infarct area compared with the other four groups (control, L-NMMA, catalase, and 8-SPT; all, $P < 0.01$). These results indicate that endogenous $H_2O_2$, in cooperation with NO, plays an important cardioprotective role in coronary I/R injury in vivo.

endothelium-derived relaxing factor; myocardial infarction; vascular endothelial function

VASCULAR ENDOTHELIAL CELLS play an important role in maintaining vascular homeostasis by synthesizing and releasing endothelium-derived relaxing factors (EDRFs), including prostacyclin ($PGI_2$), nitric oxide (NO), and endothelium-derived hyperpolarizing factor (EDHF) (6, 9, 26). Endothelial dysfunction is thus characterized by a reduction in the activity of $PGI_2$, NO, and EDHF, thereby enhancing vasoconstrictor responses mediated by endothelin, serotonin, and thrombin (26). Endothelial injury secondary to myocardial ischemia-reperfusion (I/R) decreases the production and activity of EDRFs in acute myocardial infarction (18).

Among the three different EDRFs, the roles of $PGI_2$ and NO have been extensively investigated (6, 9, 26). Regarding EDHF, since the first reports on its existence (6, 9), several candidates for EDHF have been proposed, including cytochrome *P*-450 metabolites (2, 4), endothelium-derived $K^+$ (7), and electrical communications through gap junctions between endothelial cells and vascular smooth muscle cells (29). Matoba et al. (16, 17) have previously identified that endothelium-derived $H_2O_2$ is a primary EDHF in mesenteric arteries of mice and humans. Morikawa et al. (21) have recently confirmed that endothelial Cu,Zn-SOD plays an important role as an EDHF synthase in mice. We have subsequently confirmed the importance of $H_2O_2$ in canine coronary microcirculation during coronary autoregulation with reduced coronary perfusion pressure in vivo (35).

However, it remains to be examined whether $H_2O_2$ also exerts cardioprotective effects during I/R in the coronary microcirculation in vivo, and if so, whether such effects of $H_2O_2$ compensate the impaired NO-mediated responses due to I/R injury in vivo. In this study, we tested our hypothesis that $H_2O_2$ plays an important cardioprotective and compensatory role during coronary I/R injury in dogs in vivo.

## METHODS

This study conformed to the Guideline on Animal Experiments of Kawasaki Medical School, and approved by an independent review committee from the same institution, and the *Guide for the Care and Use of Laboratory Animals* published by the National Institutes of Health.

*Animal preparation.* Anesthetized mongrel dogs (15–25 kg in body wt, $n$ = 50) of either sex were ventilated with a ventilator (model VS600, IDC, Pittsburgh, PA). Aortic pressure and left ventricular (LV) pressure were continuously monitored with a catheter (SPC-784A, Millar, TX). The blood flow of the left anterior descending coronary artery (LAD) was continuously measured by a transonic flow probe (T206, Transonic Systems, Ithaca, NY).

Address for reprint requests and other correspondence: T. Yada, Dept. of Medical Engineering and Systems Cardiology, Kawasaki Medical School, 577 Matsushima, Kurashiki, Okayama 701-0192, Japan (e-mail: yada@me.kawasaki-m.ac.jp).

The costs of publication of this article were defrayed in part by the payment of page charges. The article must therefore be hereby marked "*advertisement*" in accordance with 18 U.S.C. Section 1734 solely to indicate this fact.

*Measurements of coronary diameter by intravital microscope.* We continuously monitored coronary vascular responses by an intravital microscope (VMS 1210, Nihon-Kohden, Tokyo) with a needle probe in vivo as previously described (32). We gently placed the needle probe on subepicardial microvessels. When a clear vascular image was obtained, end-diastolic vascular images were taken with 30 pictures/s (32).

*Measurements of regional myocardial blood flow.* Regional myocardial blood flow was measured by the nonradioactive microsphere (Sekisui Plastic, Tokyo) technique, as previously described (20). Briefly, the microsphere suspension was injected into the left atrium 85 min after the onset of coronary occlusion. Myocardial collateral flow in the apex during suturing of the collateral vessels from the left circumflex artery (LCX) was calculated according to the formula: time flow = tissue counts × (reference flow/reference counts) and was expressed in milliliters per gram per minute (20).

*Detection of $H_2O_2$ and NO production.* 2′,7′-Dichlorodihydrofluorescein diacetate (DCF, Molecular Probes, Eugene, OR) and diaminorhodamine-4M AM (DAR, Daiichi Pure Chemicals, Tokyo) were used to detect $H_2O_2$ and NO production in coronary microvessels without a different NO scavenger (e.g., methylene blue), respectively, as previously described (21). Briefly, fresh and unfixed heart tissue was cut into several blocks and frozen in optimal cutting temperature compound (Tissue-Tek, Sakura Fine Chemical, Tokyo) within a few hours. Fluorescent images of [illegible] after application of ACh by using [illegible] pus BX51, Tokyo) (21). We used different animals for the [illegible] treatment (DCF and DAR) and the 2,3,5-triphenyltetrazolium chloride (TTC) treatment.

*Western blotting.* Portions of myocardial samples were homogenized in lysis buffer. After centrifugation, the supernatants were used for Western immunoblotting. The proteins were transferred by semidry electroblotting to polyvinylidene difluoride membranes. The blots were then blocked and incubated with horseradish peroxidase-conjugated rabbit anti-endothelial NO synthase (eNOS, dimer form) polyclonal antibody (Santa Cruz Biotechnology, Santa Cruz, CA) or anti-actin antibody (Santa Cruz Biotechnology). The antibody was visualized by using an enhanced chemiluminescence method (ECL; Amersham Biosciences, Tokyo). The integrated density of the bands was quantified by using NIH Image analysis, and the protein expression level of eNOS was normalized to that of actin (24).

*Experimental protocols.* After the surgical procedure and instrumentation, at least 30 min was allowed for stabilization while hemodynamic variables were monitored. The following protocols were examined.

Coronary vascular responses to endothelium-dependent [ACh, 0.5 and 1.0 μg/kg intracoronary (ic)] and -independent [sodium nitroprusside (SNP), 40 and 80 μg/min ic] vasodilators were examined before ischemia (90 min)-reperfusion (60 min) (I/R). ACh and SNP were continuously and retrogradely infused into the diagonal branch of the LAD by using a syringe pump (STC 525, Terumo, Tokyo). The coronary vascular responses to ACh and SNP were examined for 2 min, and the image of maximal vasodilatation was taken at 2 min of infusion of ACh or SNP.

Coronary vasodilator responses to ACh and SNP were examined before and after coronary ischemia (90 min)-reperfusion (60 min) by proximal LAD occlusion under the following seven conditions with cyclooxygenase blockade (ibuprofen, 12.5 mg/kg iv) to evaluate the [illegible] and NO without PGI$_2$ in a different set of animals (Fig. [illegible]-arginine (L-NMMA) [illegible] and 240,000 U·kg$^{-1}$·min$^{-1}$ ic for 10 min, an enzyme that dismutates $H_2O_2$ into water and oxygen), *4*) adenosine receptor blockade alone [8-sulfophenyltheophylline (8-SPT), 25 μg·kg$^{-1}$·min$^{-1}$ ic for 5 min], *5*) catalase plus L-NMMA, *6*) catalase plus tetraethylammonium [TEA, 10 μg·kg$^{-1}$·min$^{-1}$ ic for 10 min, an inhibitor of large-

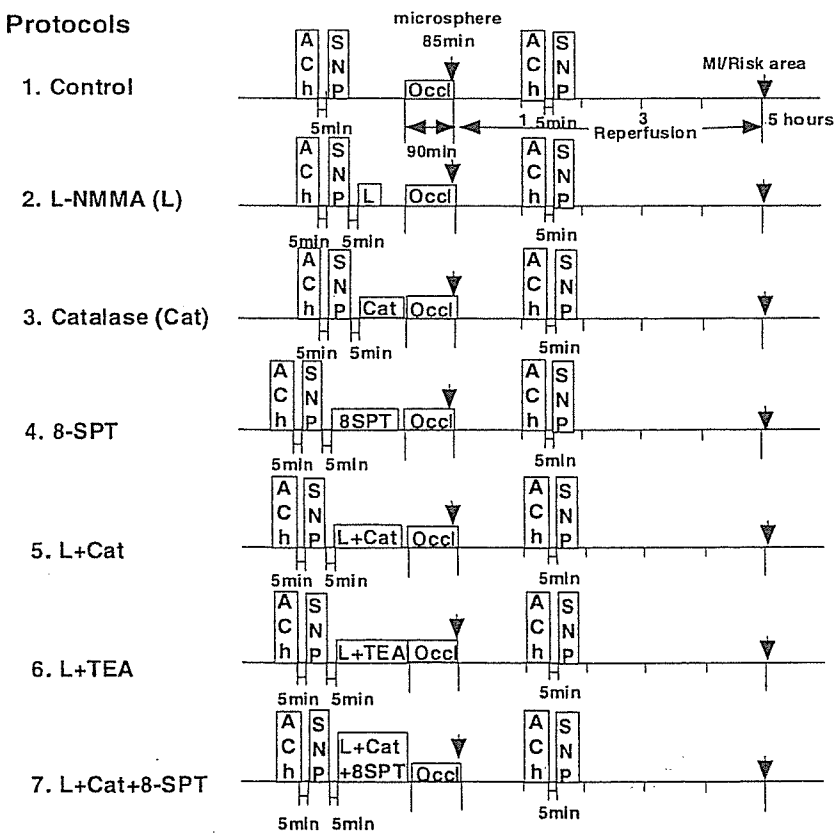


Fig. 1. Experimental protocols. TEA, tetraethylammonium; 8-SPT, 8-sulfophenyltheophylline; ACh, acetylcholine; SNP, sodium nitroprusside; Occl, coronary occlusion; Cat, catalase; L-NMMA (L), $N^G$-monomethyl-L-arginine; MI, myocardial infarction.

Table 1. *Hemodynamics during coronary ischemia-reperfusion injury in dogs*

| | | Before I/R | | | | After I/R | | |
|---|---|---|---|---|---|---|---|---|
| | *n* | Baseline | ACh | SNP | Ischemia (85 min) | Baseline | ACh | SNP |
| MBP, mmHg | | | | | | | | |
| Control | 5 | 92±4 | 91±6 | 92±5 | 93±14 | 92±4 | 91±5 | 92±6 |
| L-NMMA | 5 | 97±8 | 98±7 | 94±9 | 92±10 | 97±7 | 98±8 | 95±8 |
| Cat | 5 | 96±8 | 92±8 | 94±9 | 92±9 | 96±7 | 96±8 | 98±6 |
| L-NMMA + Cat | 5 | 94±4 | 93±9 | 97±9 | 95±11 | 95±8 | 98±5 | 94±5 |
| L-NMMA + TEA | 5 | 95±12 | 93±13 | 95±14 | 94±10 | 91±14 | 93±15 | 98±10 |
| L-NMMA + Cat + 8-SPT | 5 | 95±3 | 96±4 | 95±3 | 93±11 | 96±3 | 97±4 | 95±3 |
| Heart rate, beats/min | | | | | | | | |
| Control | 5 | 152±5 | 155±3 | 154±3 | 156±7 | 156±5 | 154±5 | 153±5 |
| L-NMMA | 5 | 157±5 | 156±5 | 157±6 | 158±6 | 153±5 | 153±5 | 153±5 |
| Cat | 5 | 155±4 | 159±6 | 158±5 | 157±6 | 151±7 | 155±8 | 154±8 |
| L-NMMA + Cat | 5 | 156±12 | 158±13 | 158±13 | 154±5 | 156±13 | 156±14 | 159±13 |
| L-NMMA + TEA | 5 | 153±13 | 154±12 | 155±11 | 155±5 | 150±10 | 151±11 | 152±10 |
| L-NMMA + Cat + 8-SPT | 5 | 152±7 | 155±9 | 153±3 | 153±5 | 152±7 | 151±6 | 153±7 |

Results are expressed as means ± SE; *n* = no. of dogs. I/R, ischemia-reperfusion; MBP, mean blood pressure; Cat, catalase; SNP, sodium nitroprusside; TEA, tetraethylammonium; 8-SPT, sulfophenyltheophylline; L-NMMA, $N^G$-monomethyl-L-arginine.

conductance $Ca^{2+}$-sensitive potassium ($K_{Ca}$) channels], and *7*) catalase plus L-NMMA with 8-SPT (35). These inhibitors were given at 30 min before I/R. An interval between each treatment was 5 min. The basal coronary diameter was defined as that before administration of ACh or SNP either before or after I/R. L-NMMA, catalase, TEA, and 8-SPT were administered alone at 5 min after administration of ACh or SNP. Microspheres were administered at 85 min after the initiation of coronary occlusion. In the combined infusion (L-NMMA + catalase + 8-SPT), catalase solution was infused into the LAD at a rate of 0.5 ml/min at 5 min after infusion of L-NMMA, and then 8-SPT was added into the LAD at 15 min after the initiation of L-NMMA.

After 1 h of reperfusion, coronary vasodilator responses to ACh and SNP were examined.

After 5 h of reperfusion, we reoccluded the LAD and injected Evans blue dye into a systemic vein. Then, myocardial slices (5 μm thick) were incubated in 1% TTC (Sigma) solution to detect the infarct area (36). Different animals were used for fluorescent treatment (DCF and DAR) and TTC treatment.

*Drugs.* All drugs were obtained from Sigma Chemical and were diluted in a physiological saline immediately before use.

*Statistical analysis.* Results are expressed as means ± SE. Vascular responses (see Figs. 3*C*, 5*F*, 6*F*, 7, and 9*A*) were analyzed by one-way ANOVA followed by Scheffé's post hoc test for multiple comparisons. Difference in the effects of ACh and SNP on subepicardial coronary microvessels before and after I/R (see Figs. 3, *A* and *B*, 4, and 8, *A* and *B*), and difference between infarct size/risk area and transmural collateral flow in control and other inhibitors (see Fig. 9*B*) were examined by a multiple regression analysis by using a model in which the change in coronary diameter was set as a dependent variable ($y$) and vascular size as an explanatory variable ($x$), while the statuses of control and other inhibitors were set as dummy variables ($D_1$, $D_2$) in the following equation: $y = a_0 + a_1x + a_2D_1 + a_3D_2$, where $a_0$ through $a_3$ are partial regression coefficients (36). The criterion for statistical significance was at $P < 0.05$.

## RESULTS

*Hemodynamics and blood gases during I/R injury.* Immediately after reperfusion, coronary blood flow was increased and some arrhythmias occurred; however, those changes returned to the control levels 1 h after reperfusion when we repeated the measurements. Thus, throughout the experiments, mean aortic pressure and heart rate at baseline were constant and comparable, and $Po_2$, $Pco_2$, and pH were maintained within the physiological ranges (pH 7.35–7.45, $Po_2 > 70$ mmHg, and $Pco_2$ 25–40 mmHg,). Hemodynamic variables at baseline did not significantly change after I/R compared with those before I/R (Tables 1 and 2).

*Dose responses to ACh and SNP.* ACh (0.5 and 1.0 μg/kg ic) and SNP (40 and 80 μg/min ic) caused coronary vasodilatation in a dose-dependent manner at both small arteries and arterioles (Fig. 2). Then we chose the maximal dose of the vasodilators (ACh, 1.0 μg/kg ic, and SNP, 80 μg/min ic) in the following experiments.

*Endothelium-dependent coronary vasodilatation before and after I/R.* There was no significant difference in baseline diameter after ACh before I/R among the groups. All inhibitors did not affect resting coronary artery diameter or coronary

Table 2. *Baseline vascular diameter before I/R in response to ACh*

| | Small Artery | Arteriole |
|---|---|---|
| Control | 104–150 μm (120±7, *n* = 7) | 37–96 μm (70±6, *n* = 12) |
| L-NMMA | 106–164 μm (131±7, *n* = 8) | 36–95 μm (63±5, *n* = 16) |
| Cat | 100–147 μm (121±5, *n* = 10) | 28–89 μm (61±6, *n* = 12) |
| 8-SPT | 114–162 μm (130±8, *n* = 6) | 30–88 μm (60±10, *n* = 5) |
| L-NMMA + Cat | 102–141 μm (118±5, *n* = 8) | 34–95 μm (77±4, *n* = 10) |
| L-NMMA + TEA | 105–142 μm (123±6, *n* = 5) | 34–95 μm (62±9, *n* = 8) |
| L-NMMA + Cat + 8-SPT | 110–145 μm (128±6, *n* = 5) | 38–87 μm (67±7, *n* = 7) |

Results are expressed as range (means ± SE); *n* = no. of blood vessels.

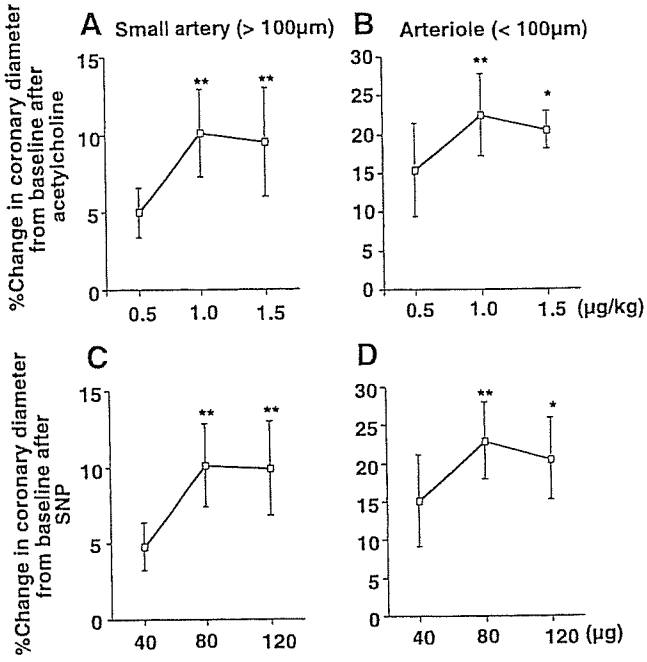


Fig. 2. Dose responses to ACh (*A* and *B*) and SNP (*C* and *D*) before ischemia-reperfusion (I/R). Number of small arteries (*A* and *C*) and arterioles (*B* and *D*) per animals used was 5/5 for each group. $*P < 0.05$, $**P < 0.01$ vs. ACh (0.5 μg/kg) and SNP (40 μg).

blood flow. Under control conditions (before I/R), intracoronary administration of ACh caused a. significantly greater coronary vasodilatation in arterioles than in small arteries (Fig. 3, *A* and *B*). Coronary I/R significantly impaired the coronary vasodilatation to ACh in both sized arteries (Figs. 3*A* and 4*A*), and L-NMMA reduced the vasodilatation in small arteries (Figs. 3*A* and 4*B*) but rather increased the response in arterioles compared with control (Figs. 3*B* and 4*A*) after I/R. Catalase and 8-SPT increased the ACh-induced vasodilatation in small arteries (Figs. 3*A* and 4, *C* and *D*) but decreased the response in arterioles (Fig. 3*B*) after I/R. There was no significant difference in coronary blood flow before and after I/R among the control, the L-NMMA, and the catalase group (Fig. 3*C*). L-NMMA + catalase (Figs. 3, *A* and *B*, and 4*E*) or L-NMMA + TEA (Figs. 3, *A* and *B*, and 4*F*) decreased the vasodilatation in both sized arteries (Fig. 3, *A* and *B*) with decrement of coronary blood flow (Fig. 3*C*), and L-NMMA plus catalase with 8-SPT further decreased the vasodilatation in both sized arteries (Figs. 3, *A* and *B*, and 4*G*) compared with other groups (Fig. 3, *A–C*).

*Detection of $H_2O_2$ and NO production.* Fluorescent microscopy with DCF showed that I/R increased the vascular $H_2O_2$ production in control LCX (Fig. 5, *B* and *F*) compared with baseline conditions (Fig. 5, *A* and *F*) and decreased the $H_2O_2$ production in control LAD (Figs. 5, *C* and *F*), which was enhanced by L-NMMA (Fig. 5, *D* and *F*) and was abolished by catalase (Fig. 5, *E* and *F*) in arterioles. By contrast, the production of NO as assessed with DAR fluorescence was increased in control LCX (Fig. 6, *B* and *F*) compared with baseline LCX (Fig. 6, *A* and *F*) after I/R, decreased in control LAD (Fig. 6, *C* and *F*), inhibited by L-NMMA (Fig. 6, *D* and *F*), and was enhanced by catalase (Fig. 6, *E* and *F*) in small arteries.

*Western blotting of eNOS protein expression in myocardium.* In the control group, expression of eNOS protein in the ischemic LAD area was significantly decreased compared with the nonischemic LCX area (Fig. 7). In the catalase group, this decrease in the eNOS protein expression was inhibited by catalase (Fig. 7).

*Endothelium-independent coronary vasodilatation.* Coronary vasodilator responses to SNP were comparable under all conditions in both sized arteries (Fig. 8). Those coronary vasodilator responses were resistant to the blockade of NO synthesis with L-NMMA (Fig. 8).

*Effect of $H_2O_2$ on I/R-induced myocardial infarct size.* I/R injury caused myocardial infarction, the size of which was ~40% of the LV risk area (Fig. 9*A*). Intracoronary L-NMMA, catalase, or 8-SPT alone did not further increase the I/R-induced infarct size (Fig. 9*A*). By contrast, intracoronary L-NMMA plus catalase or TEA markedly increased the infarct size, and L-NMMA plus catalase with 8-SPT further increased

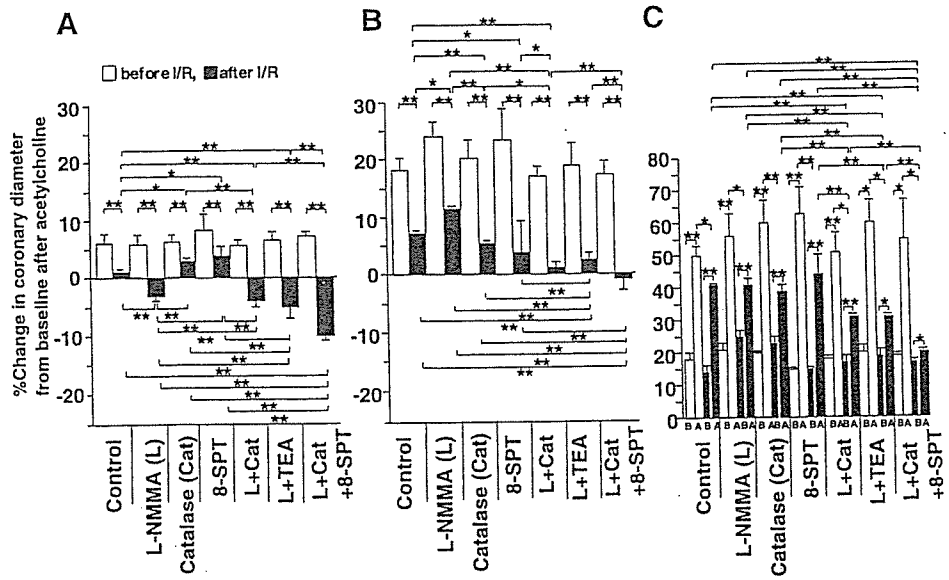


Fig. 3. Endothelium-dependent coronary vasodilatation to ACh before and after coronary I/R injury in dogs in vivo. *A*: small artery (≥100 μm). *B*: arteriole (<100 μm). *C*: coronary blood flow (CBF). No. of small arteries or arterioles per animals (*n*/*n*) used was 7/5 for control, 8/5 for L-NMMA, 10/5 for catalase, 6/5 for 8-SPT, 8/5 for L-NMMA plus catalase, 5/5 for L-NMMA plus TEA, and 5/5 for L-NMMA plus catalase plus 8-SPT in small arteries; and 12/5 for control, 16/5 for L-NMMA, 12/5 for catalase, 5/5 for 8-SPT, 10/5 for L-NMMA plus catalase, 8/5 for L-NMMA plus TEA, and 7/5 for L-NMMA plus catalase plus 8-SPT in arterioles. No. of animals during the measuring CBF used was 5 for each group. B, before ACh; A, after ACh. $*P < 0.05$, $**P < 0.01$.

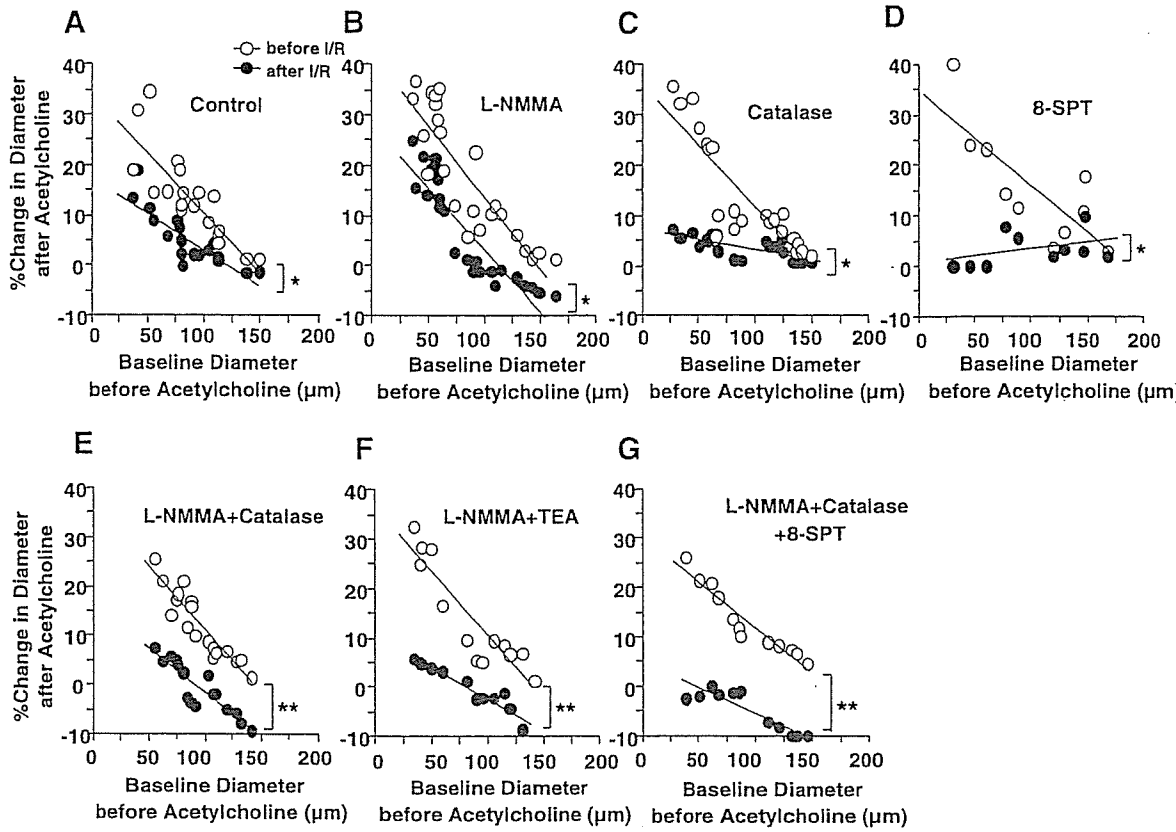


Fig. 4. Percent change in diameter after ACh before and after coronary I/R injury in dogs in vivo. No. of small arteries and arterioles per animals used was 7/5 for control (*A*), 8/5 for L-NMMA (*B*), 10/5 for catalase (*C*), 6/5 for 8-SPT (*D*), 8/5 for L-NMMA plus catalase (*E*), 5/5 for L-NMMA plus TEA (*F*), and 5/5 for L-NMMA plus catalase plus 8-SPT in small arteries (*G*); and 12/5 for control (*A*), 16/5 for L-NMMA (*B*), 12/5 for catalase (*C*), 5/5 for 8-SPT (*D*), 10/5 for L-NMMA plus catalase (*E*), 8/5 for L-NMMA plus TEA (*F*), and 7/5 for L-NMMA plus catalase plus 8-SPT in arterioles (*G*). $^*P < 0.05$, $^{**}P < 0.01$.

the infarct size (Fig. 9*A*). In the control group, there was an inverse relation between the infarct size and transmural collateral blood flow measured by microsphere technique ($r = 0.90$, $P < 0.01$). There was no significant difference in the relationship among the control, L-NMMA, and catalase treatment (Fig. 9*B*). L-NMMA plus catalase or TEA significantly shifted the regression line upward compared with the control group (both $P < 0.01$), and L-NMMA plus catalase with 8-SPT further shifted the regression line upward compared with L-NMMA plus catalase or TEA (Fig. 9*B*, both $P < 0.01$).

## DISCUSSION

The major finding of the present study is that endogenous $H_2O_2$, in cooperation with NO, plays an important cardioprotective role during coronary I/R injury as a compensatory mechanism for NO in vivo. To the best of our knowledge, this is the first report that demonstrates the important protective role of endogenous $H_2O_2$, in cooperation with NO, against coronary I/R injury in vivo.

*Validations of experimental model and methodology.* On the basis of the previous reports (22, 31), we chose the adequate dose of ACh, SNP, L-NMMA, catalase, TEA, and 8-SPT to examine the effects of endothelium-dependent and -independent coronary vasodilator responses and inhibition of NO synthesis, $H_2O_2$, $K_{Ca}$ channels, and adenosine receptor, respectively. In addition, on the basis of previous studies and our own (31, 35), we choose the doses of ACh and SNP that cause maximal coronary vasodilatation in dogs in vivo. TEA at low doses is fairly specific for $K_{Ca}$ channel, but at higher doses it may block a number of other K channels. Because several $K_{Ca}$ channels are involved in $H_2O_2$-mediated responses (26), we selected the nonselective $K_{Ca}$ inhibitor TEA to inhibit all $K_{Ca}$ channels (15). We have previously confirmed the validity of the methods that we used in the present study (32). After 60–90 min of ischemia, ultrastructural damage of coronary endothelium was observed particularly in the subendocardium in the present study, a finding consistent with the previous study (8).

*$H_2O_2$ during coronary I/R in vivo.* It was previously reported that relaxations of isolated large canine coronary arteries to exogenous $H_2O_2$ were partially endothelium dependent (23). Recently, Matoba et al. (16, 17) identified that endothelium-derived $H_2O_2$ is an EDHF in mouse and human mesenteric microvessels. Subsequently, we (35) and others (19) have confirmed that endogenous $H_2O_2$ exerts important vasodilator effects in canine coronary microcirculation in vivo and in isolated human coronary microvessels, respectively. It is conceivable that $H_2O_2$ is produced from superoxide anions derived from several sources in endothelial cells, including eNOS, cyclooxygenase, lipoxygenase, cytochrome *P*-450 enzymes, and NAD(P)H oxidases (16). In the present study, L-NMMA or catalase alone did not com-

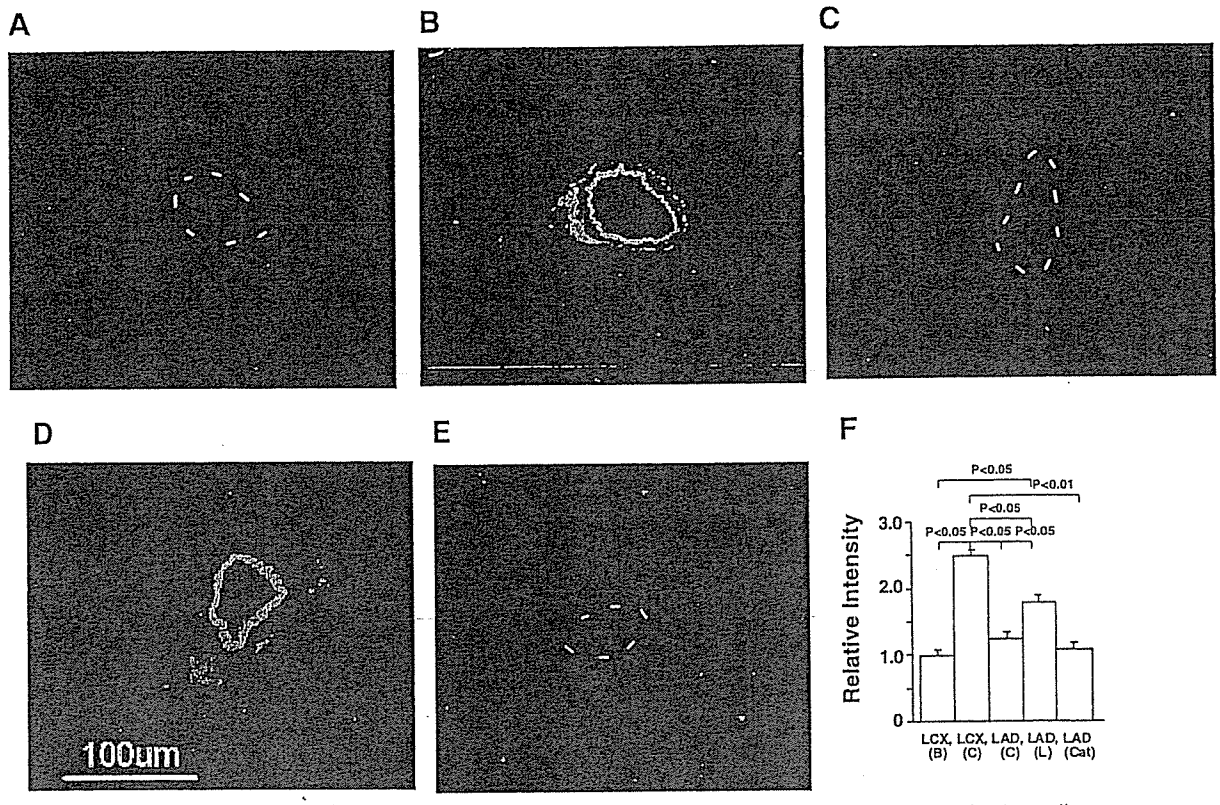


Fig. 5. Detection of $H_2O_2$ production. *A*: left circumflex artery (LCX; baseline without ACh). *B*: LCX (control). *C*: left anterior descending coronary artery (LAD; control). *D*: LAD (L-NMMA). *E*: LAD (catalase). *F*: fluorescent intensity (B, baseline without ACh; C, control, L, L-NMMA; Cat, catalase). No. of arterioles per animals used was 5/5 for each group. Dashed line, outline of vessels. Bar, 100 μm.

pletely abolish the ACh-induced vasodilatation in both sized arteries, whereas L-NMMA plus catalase markedly attenuated the residual vasodilatation in vivo as did TEA, indicating that $H_2O_2$ exerts important vasodilator effects during I/R injury in canine coronary microcirculation in vivo (Figs. 3 and 4). Furthermore, in the present study, endogenous $H_2O_2$-mediated coronary vasodilatation was noted to a greater extent in arterioles than in small arteries (Figs. 3 and 4), confirming the predominant role of $H_2O_2$ in microvessels and that of NO in relatively large arteries in vivo (25).

*Compensatory vasodilator mechanism among $H_2O_2$, NO, and adenosine.* It is well known that coronary vascular tone is regulated by the interactions among several endogenous vasodilators, including NO, $H_2O_2$, and adenosine (33). These vasodilators play an important role in compensatory vasodilatation of coronary microvessels during myocardial ischemia (35). In the present study (Figs. 3 and 4), endothelium-dependent arteriolar vasodilatation to ACh during coronary I/R was significantly increased by L-NMMA while small arterial vasodilatation to ACh was increased by catalase and 8-SPT, and the residual arteriolar dilation was further inhibited by both of them (L-NMMA plus catalase or TEA). Furthermore, fluorescent microscopy with DCF and DAR, respectively, showed that $H_2O_2$ and NO production after I/R were enhanced in small coronary arteries and arterioles by L-NMMA [fluorescent intensity (FI) 1.8] and catalase (FI 1.9) compared with those in the LAD of control group (Figs. 5 and 6, FI: DAR 1.2 and DCF 1.1). The residual small arteriolar dilatation after combined administration of L-NMMA + catalase was completely blocked by 8-SPT, an adenosine receptor blocker, indicating that adenosine also compensated for the loss of action of NO and $H_2O_2$. Taken together, these results indicate the compensatory vasodilator effects among NO, $H_2O_2$, and adenosine to maintain coronary blood flow during coronary I/R injury in vivo. $H_2O_2$ and NO were mutually compensatory in both small arteries and arterioles, and in the presence of their inhibitors (catalase and L-NMMA), adenosine also caused arteriolar vasodilatation, as we reported previously (35). This finding is consistent with our finding that NO, $H_2O_2$, and adenosine play an important compensatory role in coronary autoregulation in canine coronary microcirculation in vivo (35). It was reported that TEA inhibited adenosine-induced vasodilatation of canine subepicardial coronary arteries in vitro (3). Furthermore, $H_2O_2$ stimulates protein kinase C, phospholipase $A_2$, and arachidonic acid release and increases intracellular cAMP levels (10). These findings suggest that cAMP-mediated pathway is involved, at least in part, during coronary vasodilatation through $K_{Ca}$ channels after I/R injury.

*Role of $H_2O_2$ during coronary I/R.* It is known that $K_{Ca}$ channels substantially contribute to coronary vasodilatation in myocardial ischemia (22) and that $H_2O_2$ also activates $K_{Ca}$ channels (11). However, it remains to be examined whether $H_2O_2$ contributes to coronary vasodilatation during I/R in vivo. The present results demonstrate that $H_2O_2$

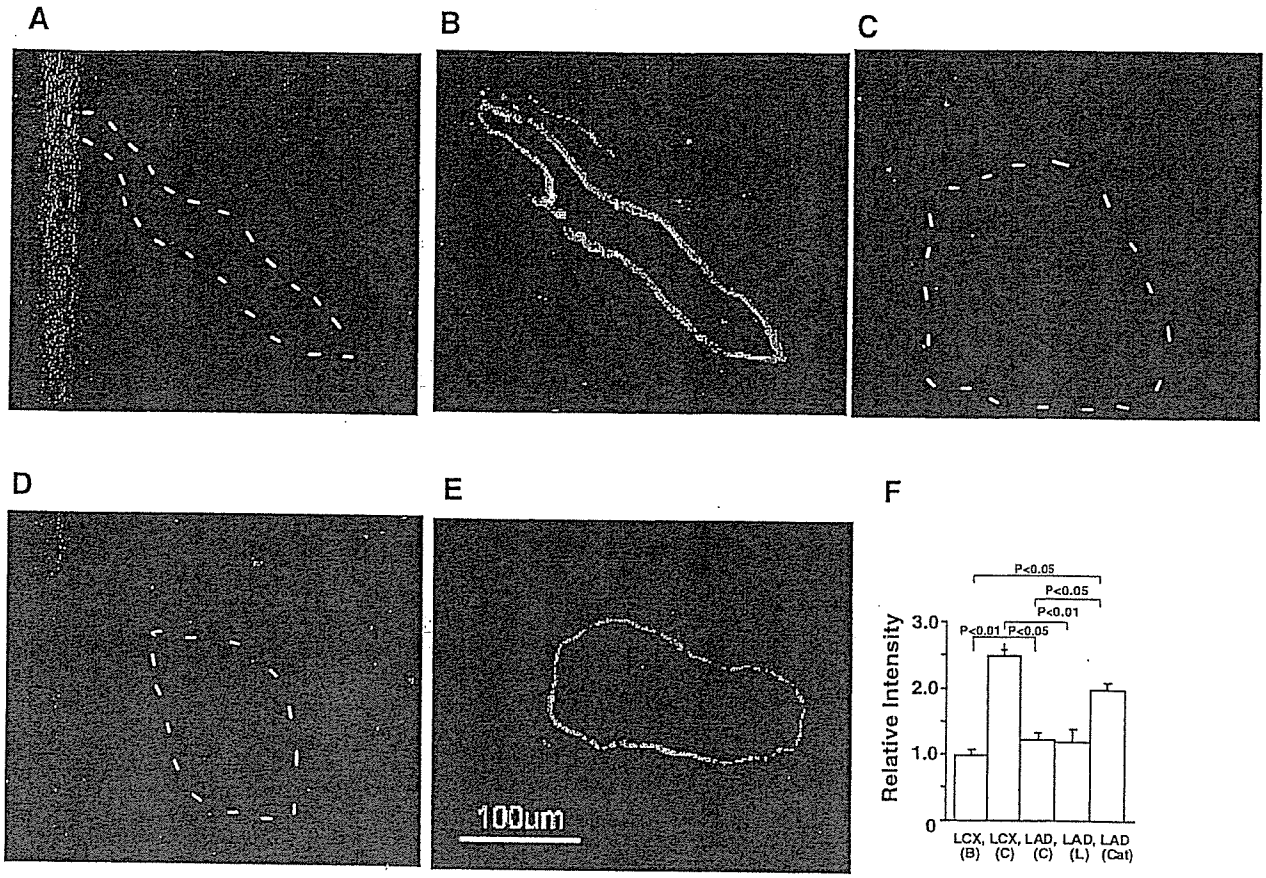


Fig. 6. Detection of nitric oxide (NO) production. *A*: LCX (baseline without ACh). *B*: LCX (control). *C*: LAD (control). *D*: LAD (L-NMMA). *E*: LAD (catalase). *F*: fluorescent intensity (B, baseline without ACh; C, control, L, L-NMMA; Cat, catalase). No. of small arteries per animals used was 5/5 for each group. Dashed line, outline of vessels.

substantially contributes to coronary vasodilatation during I/R in vivo as a compensatory mechanism for the loss of NO. Several mechanisms have been proposed for $K_{Ca}$ channel opening during coronary I/R, including cellular acidosis

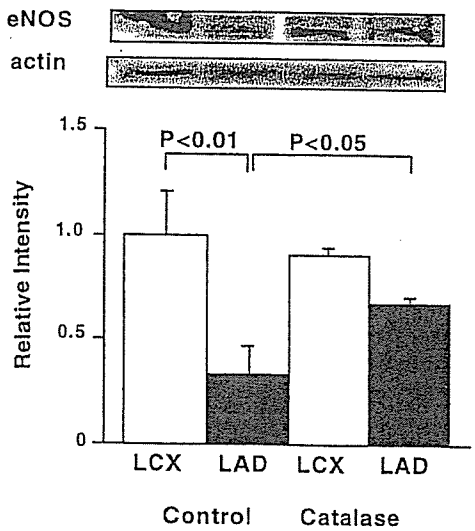


Fig. 7. Western blotting showing the effects of catalase on endothelial nitric oxide synthase (eNOS) protein expression in the myocardium of LAD and LCX. No. of animals used was 3 for each group.

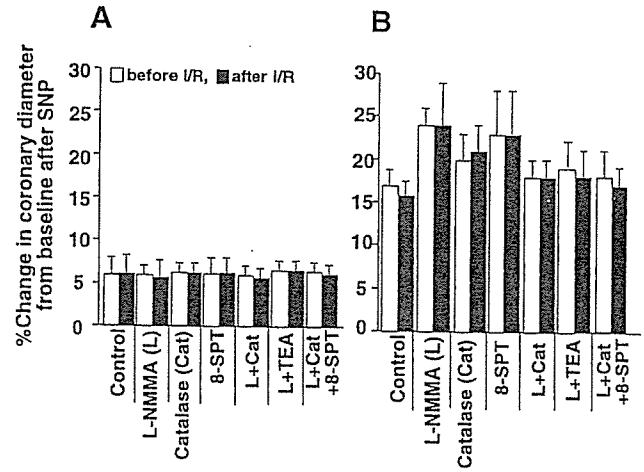


Fig. 8. Endothelium-independent coronary vasodilatation before and after coronary I/R injury in dogs in vivo. *A*: small artery ($\geq$100 μm). *B*: arteriole (<100 μm). No. of small arteries and arterioles per animals used (*n*/*n*) was 7/5 for control, 8/5 for L-NMMA, 10/5 for catalase, 6/5 for 8-SPT, 8/5 for L-NMMA plus catalase, 5/5 for L-NMMA plus TEA, and 5/5 for L-NMMA plus catalase plus 8-SPT in small arteries; and 12/5 for control, 16/5 for L-NMMA, 12/5 for catalase, 5/5 for 8-SPT, 10/5 for L-NMMA plus catalase, 8/5 for L-NMMA plus TEA, and 7/5 for L-NMMA plus catalase plus 8-SPT in arterioles.

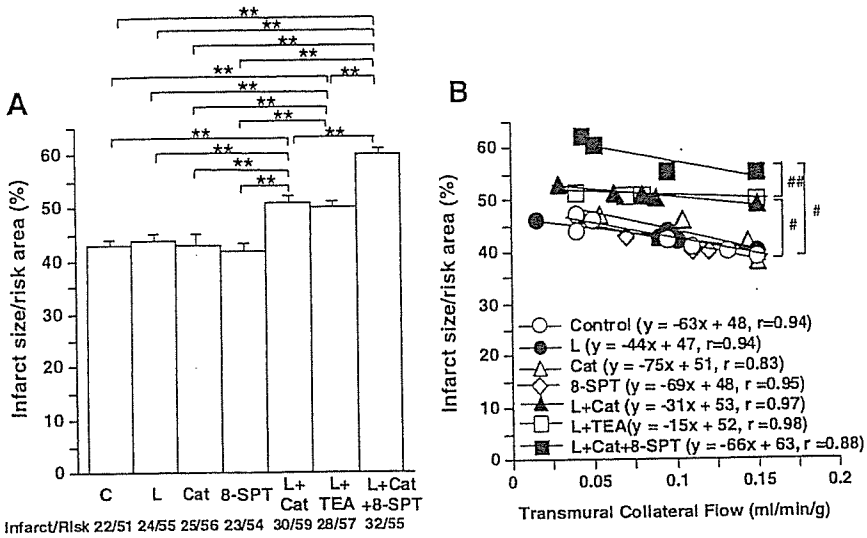


Fig. 9. Effects of $H_2O_2$, NO, and adenosine on I/R-induced MI in dogs in vivo. *A*: I/R-induced left ventricular infarct size in dogs in vivo. C, control. *B*: plot of infarct size expressed as a percentage of the risk area and regional collateral flow during I/R. $^{**}P < 0.01$, $\#P < 0.05$ vs. L-NMMA (L) or Cat or 8-SPT; $\#\#P < 0.01$ vs. L + TEA or L + Cat.

(27), increase in intracellular $Ca^{2+}$ concentration after ischemia (28), and $H_2O_2$ production by inflammatory cells (5). Furthermore, an inhibitor of NO synthesis [$N^G$-nitro-L-arginine methyl ester (L-NAME)] or that of $K_{Ca}$ channels (charybdotoxin) partly inhibits the protective effect on myocardial infarct size (22). Liu et al. (14) demonstrated that peroxynitrite inhibits $K_{Ca}$ channel activity in human coronary arterioles during I/R. This mechanism might contribute to impaired $H_2O_2$-mediated dilation in I/R where NO synthase activity is increased in the presence of excess of $O_2^-$. In the present study, inhibition of $H_2O_2$ or NO alone did not significantly increase myocardial infarct size compared with control conditions (Fig. 9). These results suggest that $H_2O_2$ and NO exert cardioprotective effects against the development of myocardial infarction in a compensatory manner.

Recently, we have demonstrated that the expression of eNOS protein is decreased in the ischemic myocardium, which is improved by a selective Rho-kinase inhibitor, hydroxyfasudil, during coronary I/R injury in dogs in vivo (36). Furthermore, a physiological concentration (2 μmol/l) of $H_2O_2$ improved the recovery of both cardiac contractile function and energy metabolism after I/R in perfused rat heart (37). In the present study, the expression of eNOS protein was decreased in the ischemic myocardium, which was increased by catalase during I/R injury (Fig. 7). All these mechanisms may be involved in the beneficial effects of $H_2O_2$ on the I/R-induced myocardial injury. It also is conceivable that I/R reduces endothelial tetrahydrobiopterin levels in coronary vessels and impairs eNOS function (30).

*Limitations of the study.* Several limitations should be mentioned for the present study. First, we did not examine coronary vasodilatation in response to SOD/SOD mimetic (e.g., Tempol) or peroxynitrite inhibitor (e.g., ebselen) after I/R. However, because of the complex interactions among the oxygen species, we consider that both Tempol and ebselen also affect $H_2O_2$ metabolism by scavenging superoxide anions and peroxynitrite, respectively. Second, in addition to catalase, endogenous glutathione peroxidase (GSH) also plays an important role in removing $H_2O_2$, and NO also could be a substrate for endogenous catalase (1). However, in the present study, we used exogenous catalase to remove $H_2O_2$ to examine the role of the reactive oxygen species. Third, the exact source of vascular $H_2O_2$ production remains to be elucidated (e.g., the endothelium, smooth muscle, or cardiomyocytes). Fourth, while we were able to demonstrate the production of $H_2O_2$ using fluorescent microscopy with DCF, we were unable to quantitatively measure the $H_2O_2$ production because DCF detects $H_2O_2$, $ONOO^-$, and HOCl as well. Fifth, we were unable to find smaller arterioles because of the limited spatial resolution of our CCD intravital microscope. If we had an intravital camera with higher resolution, we would be able to observe coronary vasodilator responses of smaller arterioles.

*Clinical implications and conclusions.* During coronary I/R, microemboli of atherosclerosis debris and platelet plugs are released into the coronary microcirculation, particularly at revascularization with thrombolysis and/or percutaneous coronary intervention. Thus preexisting coronary endothelial dysfunction with various risk factors may be an important determinant for I/R injury in acute myocardial infarction. The synthesis and/or action of endothelium-derived NO are impaired under various pathological conditions, such as hypertension, hyperlipidemia, and diabetes mellitus (26, 34). In hypertension, K channel activities are increased in a compensatory manner with reduced NO activity (13). The present results suggest that NO and $H_2O_2$ compensate each other to cause coronary vasodilatation during I/R injury in vivo.

In conclusion, we were able to demonstrate that endogenous $H_2O_2$, in cooperation with NO, plays an important cardioprotective role in coronary I/R injury in vivo. The present findings may have important clinical implications because $H_2O_2$-mediated mechanisms substantially contribute to endothelium-dependent vasodilatation in coronary I/R in vivo.

## GRANTS

This work was supported in part by grants from the Japanese Ministry of Education, Science, Sports, Culture, and Technology, Tokyo, Japan (Nos. 13307024, 13557068, 14657178, 15256003, 16209027, 16300164), and the Program for Promotion of Fundamental Studies in Health Sciences of the Organization for Pharmaceutical Safety and Research of Japan.